Borehole Seismic Observations From the Chicxulub Impact Drilling: Implications for Seismic Reflectivity and Impact Damage

C. G. Nixon, D. R. Schmitt, R. Kofman, J. Lofi, S. P. S. Gulick, S. Saustrup, G. L. Christeson, D. A. Kring

Geochemistry, Geophysics, Geosystems®

AGU ADVANCING EARTH AND SPACE SCIENCE

RESEARCH ARTICLE
10.1029/2021GC009959

Key Points:

- We present analyses from a vertical seismic profile at Site M0077 on the Chicxulub peak ring
- Reflectivity is primarily from a low velocity zone of hydrothermally altered impactites at the top of the peak ring below Cenozoic sediments
- We derive *Grady-Kipp* damage parameters and Poisson's ratios which indicate high damage levels within the peak ring

Supporting Information:

Supporting Information may be found in the online version of this article.

Correspondence to:

C. G. Nixon,
cnixon@ualberta.ca

Citation:

Nixon, C. G., Schmitt, D. R., Kofman, R., Lofi, J., Gulick, S. P. S., Saustrup, S., et al. (2022). Borehole seismic observations from the Chicxulub impact drilling: Implications for seismic reflectivity and impact damage. *Geochemistry, Geophysics, Geosystems*, *23*, e2021GC009959. https://doi.org/10.1029/2021GC009959

Received 8 JUN 2021
Accepted 12 NOV 2021

Author Contributions:

Conceptualization: C. G. Nixon, D. R. Schmitt, R. Kofman, J. Lofi, S. P. S. Gulick, G. L. Christeson, D. A. Kring
Data curation: C. G. Nixon, S. Saustrup
Formal analysis: C. G. Nixon, D. R. Schmitt, J. Lofi, S. Saustrup, G. L. Christeson
Funding acquisition: D. R. Schmitt
Investigation: C. G. Nixon, D. R. Schmitt, R. Kofman, J. Lofi, S. P. S. Gulick, S. Saustrup, G. L. Christeson, D. A. Kring

Borehole Seismic Observations From the Chicxulub Impact Drilling: Implications for Seismic Reflectivity and Impact Damage

C. G. Nixon[1], D. R. Schmitt[1,2], R. Kofman[1], J. Lofi[3], S. P. S. Gulick[4,5,6], S. Saustrup[4], G. L. Christeson[4], and D. A. Kring[7]

[1]Department of Physics, University of Alberta, Edmonton, AB, Canada, [2]Department of Earth, Atmospheric and Planetary Science, Purdue University, West Lafayette, IN, USA, [3]Géosciences Montpellier, Université de Montpellier, Montpellier, France, [4]Institute for Geophysics, Jackson School of Geosciences, University of Texas at Austin, Austin, TX, USA, [5]Department of Geological Sciences, Jackson School of Geosciences, University of Texas at Austin, Austin, TX, USA, [6]Center for Planetary Systems Habitability, University of Texas at Austin, Austin, TX, USA, [7]Lunar and Planetary Institute, Houston, TX, USA

Abstract We conducted a vertical seismic profile (VSP) in the borehole of International Ocean Discovery Program/International Continental Scientific Drilling Program Expedition 364 Site M0077 to better understand the nature of the seismic reflectivity and the in situ seismic properties associated with the Chicxulub impact structure peak ring. Extraction of the up-going wavefield from the VSP shows that a strong seismic reflection event imaged in seismic reflection data results from discontinuities in the elastic impedance Z (the product of density and wave speed) at the top and bottom of a zone of hydrothermally altered melt-bearing polymict breccia (suevite) that are characterized by anomalously low Z. Below this strong carbonate/suevite reflection event, the upgoing seismic wavefield is chaotic, indicating high levels of scattering from the suevites and underlying melt rocks and shocked granitoids of the peak ring, in contrast to the clear coherent reflections throughout the overlying Cenozoic sediments. We extract shear wave speeds, which, together with those provided from the complementary sonic log and densities from core scanning, allowed determination of V_P/V_S and Poisson's ratio ν. These values are anomalously high relative to comparable terrestrial lithologies. We also calculate a variety of damage parameters for the disrupted peak ring granitoids. These values may assist in linking seismic observations to shock levels that are necessary to calibrate current impact models and may also be useful in assessing levels of fracturing within major fault zones.

Plain Language Summary Seismic profiling over geological features reveal to us both the geometry of the structure and the speeds of the seismic waves within it. Calibrating these profiles using only data from the surface, however, remains challenging, but this can be accomplished by making direct seismic measurements in a borehole with a technique called vertical seismic profiling (VSP). Here, we describe the analysis of such a VSP acquired during drilling into the Chicxulub Impact Structure during International Ocean Discovery Program Expedition 364. Special processing of the waves confirm that the strong seismic reflection seen in surface data originates from abrupt changes in the rock properties related to the juxtaposition of hardened sediments, weak suevites, and melt rock. No seismic reflections could be found originating deeper in the uplifted and highly damaged granitoids of the structures's peak ring. As noted in earlier studies, the seismic wave speeds are anomalously low in these lower materials. These speeds were converted into damage indexes and as such this information may provide a means toward constraining advanced numerical impact modeling and in assessing levels of damage in the subsurface in advance of construction on the surfaces of the Moon and Mars.

1. Introduction

Complex impact structures are common throughout the solar system and their relatively uneroded surface morphologies have been well studied on the extraterrestrial planets and natural satellites (Phillips et al., 1991; Pike & Spudis, 1987; Wood & Head, 1976). However, spaceborne remote sensing can only reveal extremely limited details of the subsurface of these craters, such as geological structure or physical properties. These elusive details can elucidate the dynamics of the formation of complex impact structures and are particularly important for the largest impact structures (impact basins) which exhibit peak rings (Melosh, 1989). Geophysical and

Methodology: C. G. Nixon, D. R. Schmitt, R. Kofman, J. Lofi, S. P. S. Gulick, S. Saustrup, G. L. Christeson
Project Administration: D. R. Schmitt, J. Lofi, S. P. S. Gulick
Resources: D. R. Schmitt
Software: C. G. Nixon, D. R. Schmitt
Supervision: D. R. Schmitt, J. Lofi
Validation: C. G. Nixon, D. R. Schmitt, S. P. S. Gulick, G. L. Christeson, D. A. Kring
Visualization: C. G. Nixon, D. R. Schmitt, S. P. S. Gulick, G. L. Christeson
Writing – original draft: C. G. Nixon, D. R. Schmitt
Writing – review & editing: C. G. Nixon, D. R. Schmitt, R. Kofman, J. Lofi, S. P. S. Gulick, G. L. Christeson, D. A. Kring

drilling investigations from the bodies' surface can provide this information, but due to the active hydrological and tectonic cycles acting on weak shock-damaged, faulted rock masses with initially steep topography, there is only one confirmed intact peak-ring structure on Earth (Kenkmann et al., 2014). The ~200 km diameter Chicxulub impact structure's peak ring is fortuitously preserved by nearly continuous limestone blanketing on a geologically stable passive margin since its formation (Lopez Ramos, 1975). As such, the accessible Chicxulub structure presents opportunities for direct geophysical and sampling investigations to further constrain our understanding of the formation of such structures. Our study focuses on understanding the nature of the seismic wavefield within peak rings through detailed Hole M0077A seismic observations carried out as a component of the International Ocean Discovery Program (IODP)/International Continental Scientific Drilling Program (IODP/ICDP) Expedition 364 Chicxulub drilling project located off the Yucatán Peninsula, México (Figure 1).

Active source seismic profiling has been extensively used in imaging of impact craters since the first focused refraction studies at the complex Ries Crater as early as 1948 (Angenheister and Pohl, 1976) and at the simple Meteor Crater, Arizona in the 1970s (Ackermann et al., 1975). On Earth, complex craters in crystalline targets are typically >4 km in diameter but can have diameters as low as 2 km in softer sedimentary rocks (French & Hokett, 1998; Melosh, 1989). Complex craters include a central uplift zone, a melt sheet, and a normal faulted rim where large blocks slumped into the transient crater (French & Hokett, 1998; Melosh, 1989). Active source seismological profiles exist over a number of complex craters, an incomplete listing of which includes the Chesapeake Bay Structure (Catchings et al., 2008), Mjølnir crater, North Sea (Gudlaugsson, 1993), Siljan structure, Sweden (Juhlin & Pedersen, 1987), Upheaval Dome, Utah (Kanbur et al., 2000), Manson Structure, Iowa (Keiswetter et al., 1996), Bosumtwi Structure, Ghana (Scholz et al., 2002), El'gygytgyn Structure, Siberia (Niessen et al., 2007), Haughton Structure, Nunavut (Scott & Hajnal, 1988), Sudbury Structure, Ontario (Wu et al., 1995), and Bow City Structure, Alberta (Glombick et al., 2014). The seismic profiles obtained in these studies are consistent with central uplifts and faulted rims of larger complex craters (Melosh, 1989).

To date, the VSP data obtained during the Expedition 364 Chicxulub drilling program have been used in obtaining in situ compressional seismic wave speeds, V_P (Christeson et al., 2018). However, VSP data can also calibrate the depth to reflectors, improve the understanding of the nature of the seismic wavefield in the complex structure, resolve the details of the reflectivity, and provide additional constraints on the in situ physical properties. Here, we extend the VSP data set to better understand the nature of the seismic reflectivity of the Chicxulub peak ring, overlying impactites, and K-Pg boundary sequence including displaced target rocks (Gulick et al., 2019; Morgan et al., 2016) and to obtain estimates of shear wave speeds, V_S, to contribute to understanding the unique geological formations produced during large impacts. Additionally, obtaining measures of the seismic wavefield within the highly damaged rock masses of large impact structures may provide additional insight into the anomalous 'diffusive' seismic wave propagation on the Moon (e.g., Dainty & Toksoz, 1977; Latham et al., 1970; Pandit & Tozer, 1970) or assist in the interpretation of seismic observations on Mars (e.g., Karakostas et al., 2020; Lognonne et al., 2020).

We begin with an overview of the geological and physical properties found at Site M0077 and of the VSP methodology, provide the results of the structural measurements, and interpret these results with regard to the high degree of shock deformation experienced by the displaced crystalline peak ring materials as well as longer term processes that modified the seismic properties. The wave speeds, observed both in sonic logs and directly from the VSP data, are contrasted against comparable terrestrial analogs. Finally, we derive measures of damage that may be used as metrics in the assessment of deformations predicted by hydrocode impact modeling codes.

2. Background

2.1. Chicxulub Structure

The Chicxulub impact structure is centered near the village of Puerto Chicxulub on the Yucatán platform, México. The platform is characterized offshore by carbonate and evaporite depositional facies (Gischler & Lomando, 1999) and onshore by an unconfined flat laying karstic environment (Weide & Faber, 1985). Active source seismic source marine profiling (Camargo-Zanoguera & Suarez-Reynoso, 1994; Gulick et al., 2008; Hildebrand et al., 1998; Morgan et al., 1997) and passive monitoring (Campos-Enriquez et al., 2004; Mackenzie et al., 2001) have provided data used in numerous subsequent analyses: reflection for structure (Bell et al., 2004; Christeson et al., 2018; Gulick et al., 2008) and refraction for velocities (Christeson et al., 2001, 2009); these

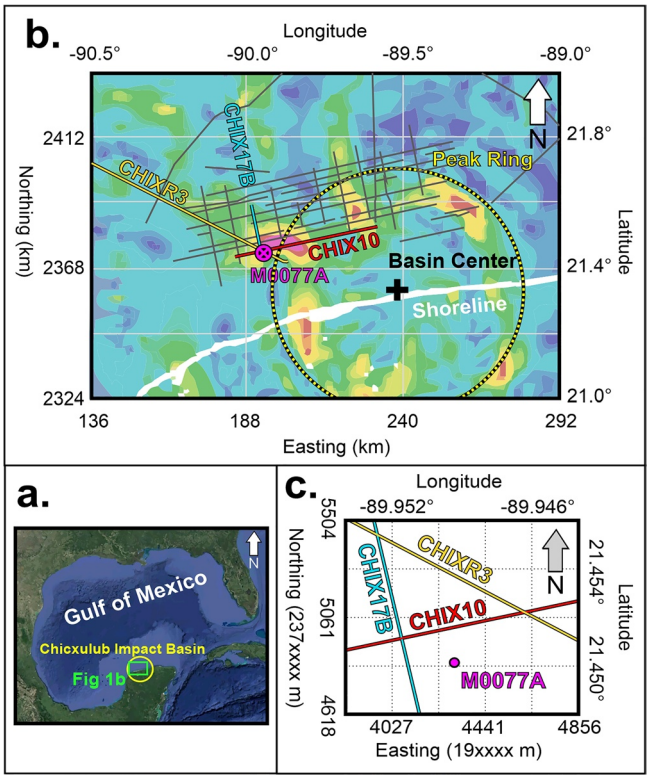

Figure 1. 1 Location of Chicxulub structure (a) Within the Gulf of Mexico (b) With radius of the peak ring from the basin center and the nearby surface seismic profiles superimposed on horizontal gravity gradient map after (Hildebrand et al., 1998). (c) Project Hole M0077A in purple compared to nearby seismic lines, located in UTM zone Q16 N. Northing is 2,370,000 + *y*-axis, Easting is 190,000 + *x*-axis.

studies are described in recent reviews by Canales-Garcia et al. (2018), Gulick et al. (2013), and Salguero-Hernández et al. (2020). Together with the knowledge available from prior regional drilling (Lopez Ramos, 1975), these data are consistent with an interpretation that the Chicxulub structure is a complex crater which include elements (Figure 2) consisting of structural uplift with: (a) a ~30 km diameter central zone of uplifted lower and mid crustal rocks blanketed by impactites and a thick melt sheet of near 40 km radius, (b) a topographically high peak ring of upper- and mid-crustal materials displaced upwards and coated with a thin veneer of melt and suevite, and (c) a series of terraced slump blocks of the upper crust and the original Mesozoic platform sediments that collapsed inward during the crater modification stage. This terrace zone bounds and lies beneath an annular trough filled with impactites and melt rock that extends to ~75 km radius, interpreted as the crater rim (Morgan et al., 2000) or inner rim considering the existence of additional ring structures such as offset sediments that define an outer ring at ~100 km radius (Gulick et al., 2008). The Chicxulub structure of Figure 2 is consistent with locations where large displacements may occur in numerical hydrodynamic crater modeling (Collins et al., 2008).

A portion of the seismic profile line CHIX10 (Figure 2b) is interpreted following Christeson et al. (2018), with detailed rationales provided by Gulick et al. (2008). The profile's features include: (a) the layered Cenozoic sediments deposited since the impact, (b) a strong and continuous event present across the profile confirmed by the drilling to be associated with the upper K-Pg boundary, (c) the peak-ring formed by uplift and dynamic collapse of the central uplift immediately following the K-Pg impact, (d) suevite bounding and capping the peak-ring, and (e) a thick zone of melt rock within the central basin, the top of which is delineated by an irregular low frequency reflector. The Suevite/Transitional Unit Contact (STUC) at 617.33 mbsf is a disconformity delineating the transition from rapid suevite deposition to Paleogene marine sedimentation, with the iridium layer being present at 616.6 mbsf (Goderis et al., 2021) and thus marking the top of the K-Pg boundary sequence within the crater. Within the peak-ring, a continuous low frequency and irregular reflector (LFR) lies below the STUC with a 130 m layer of suevite and melt rock in between as drilled at Site M0077 (Gulick et al., 2019; Morgan et al., 2017). This LFR has been associated, albeit intermittently, with the base of a thin zone of low velocity found by full waveform inversion (Morgan et al., 2011). Aside from the LFR, there are no laterally coherent reflections within the peak ring, although, numerous diffraction hyperbolae in the time migrated stack indicate a complex scattering regime.

The character in the 2D surface profiles below the Chicxulub suevite is non-reflective; as there are no laterally coherent events visible, these zones are often said to be "seismically transparent", meaning that there are no readily traceable coherent events visible. Aside from impact structures (e.g., Scholz et al., 2002), seismic imaging over metamorphic crystalline cratons (e.g., Kneib, 1995) and igneous basalt flows are examples of geological environments that exemplify "seismically transparent" sections.

Overall, the seismic observations are consistent with the "dynamic collapse" model (Collins et al., 2002, 2008; Ivanov & Kostuchenko, 1997), which accounts for the uplift and subsequent collapse of the central peak as well as the overturning of basement crust on top of the slump blocks of Mesozoic sediments to form the peak ring (Collins et al., 2002; Morgan et al., 2016). The peak ring in situ densities and seismic wave speeds as determined from gravity modeling and seismic tomographic inversion are significantly diminished relative to the values expected for intact crystalline cratonic crustal rock (Christeson et al., 2018). Resolving this discrepancy from what is expected for the depths of origin of the peak ring rocks and testing the dynamic collapse hypothesis against competing models for the formation of peak ring structures in part motivated Expedition 364 (Site M0077) drilling and sampling of Chicxulub's peak ring in 2016. The borehole stratigraphy is composed of post-impact Cenozoic carbonates overlying impactites, which in turn overlie highly fractured and shock damaged felsic granitoid

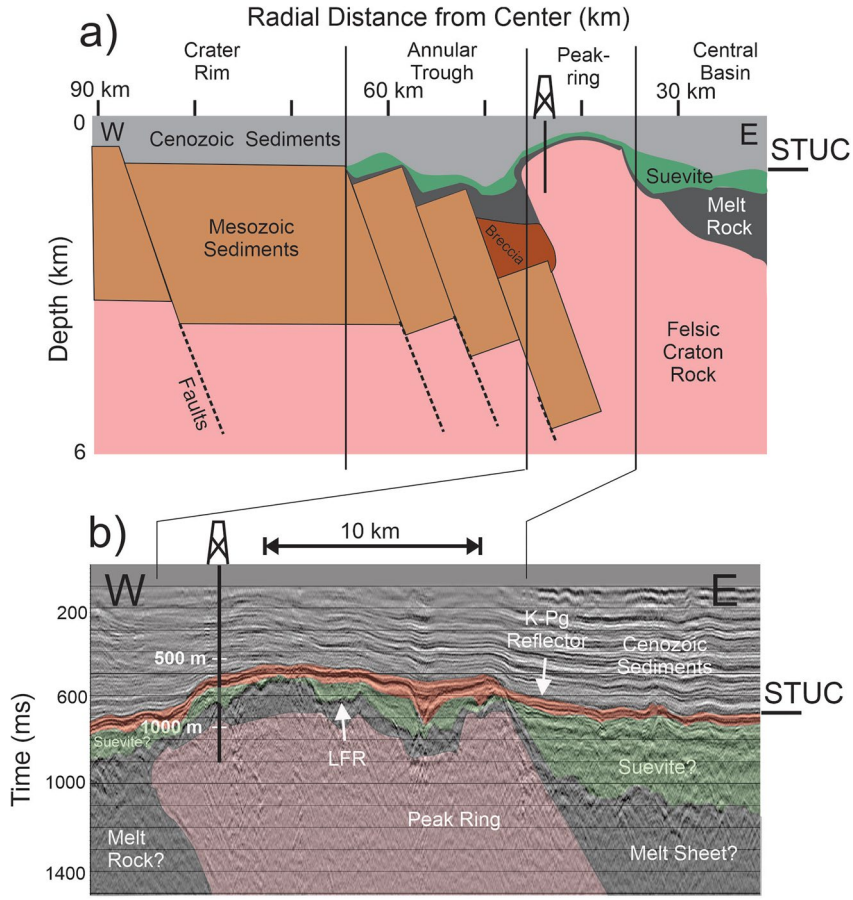

Figure 2. (a) Conceptual geological cross section with upper contact of K-Pg boundary layer demarked by the Suevite/Transitional Unit Contact (STUC) along radius from crater center adapted from the interpretations of Vermeesch and Morgan (2008), Morgan et al. (2011), and Gulick et al. (2013), updated from Expedition 364 observations following Simpson et al. (2020), and suevite/melt rock/breccia transitions updated from Christeson et al. (2021). (b) Portion of the migrated stack of line CHIX10 (Gulick et al., 2008) over the peak-ring with the K-Pg reflector highlighted in red and the underlying low frequency reflector (LFR) indicated. Closest offset of Expedition 364 borehole M0077 A from Line 10 indicated by small drill rig with depth extent correlating to 2-way time of 890 ms.

basement blocks interspersed with impact melt and breccia dikes (Morgan et al., 2017). The composition of the felsic basement rocks is consistent with numerical modeling results, which suggests these materials originated at a depth of ~10 km and were displaced laterally more than 20 km to form the peak ring. Both the low densities and seismic wave speeds of these felsic rocks correlate with their anomalously high porosities (Christeson et al., 2018) produced during shock compression to pressures possibly as high as 20 GPa (Feignon et al., 2020; Morgan et al., 2016; Rae et al., 2019). These low wave speeds were clearly observed by full waveform seismic tomography inversion (Christeson et al., 2021; Morgan et al., 2011) and were confirmed by both downhole sonic logging and the zero-offset VSP from Expedition 364 discussed in more detail here.

2.2. Expedition 364 Geology

Site M0077 (Figure 1c) was drilled during the joint IODP/ICDP Expedition 364 campaign in 2016 at a location estimated to be ~46 km from the center of the impact structure. Summaries of the technical details of the project may be found in (Gulick et al., 2017a), of the geophysical logging in (Lofi et al., 2018), and of the combined log/core property interpretation in (Christeson et al., 2018; See Table S1 in Supporting Information S1). The borehole was drilled in three stages, dependent upon engineering and key target considerations, with cores obtained between 505.7 and the total depth of the hole at 1334.7 m below sea floor (mbsf; Morgan et al., 2017). The core was classified based on lithology into four major lithostratigraphic, units 1 through 4,

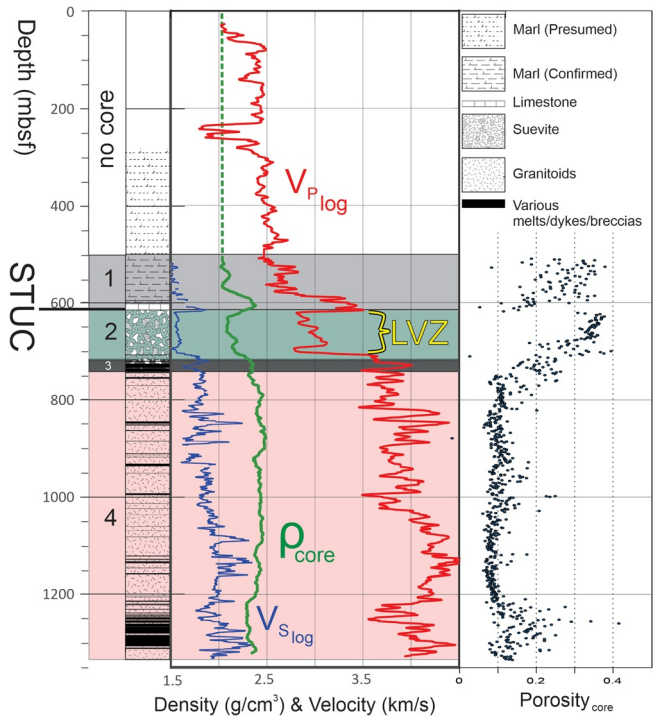

Figure 3. Simplified geological column from core and cuttings with the four major units as interpreted from the core (505.7 mbsf to 1334.7 mbsf) compared to running average of density measurements on discrete core samples (green line) and to the running average over 0.5 m of the P-wave (red line) and S-wave (blue line) speeds as measured by the sonic log. Core was not retrieved above 500 m and so it is not included in the 4 colored units.

that are broadly characterized as post-impact sediments, suevite, impact melt rock, and displaced shocked granitoids, respectively (Smith et al., 2020). Unit 1 (505.7–617.33 mbsf) consists of post-impact Paleogene and Eocene pelagic limestones, marls, and claystones, extending to the STUC at 617.33 mbsf. Directly above the STUC is Transitional Unit 1G (616.58–617.33 mbsf), which is a micritic limestone likely deposited over a period of a few years (Gulick et al., 2019; Lowery et al., 2018; Whalen et al., 2020), capped by the K-Pg iridium anomaly (Goderis et al., 2021). The approximately 55.93–55.71 Ma Paleogene-Eocene Thermal Maximum manifests as a thin (607.27–607.06 mbsf) shale layer bounded by a disconformity to Paleogene carbonate 'hardground' below and bioturbated limestones above (Smith et al., 2020). The Palynological age-depth relationships show low sedimentation rates of 0.22 cm/Kyr on average over the Paleocene section, complicated by numerous unconformities, with high average rates of 2.3 cm/Kyr through the Eocene section (Gulick et al., 2017e).

Lithostratigraphic Unit 2 (617.33 mbsf to 721.61 mbsf) and Unit 3 (721.61 mbsf to 747.02 mbsf) are an ~130 thick series of impactites deposited immediately following the excavation, rebound, and dynamic collapse of the crater. The upper ~90 m is suevite with generally decreasing particle sizes upwards indicative of rapid deposition of materials carried by ocean resurge into the crater in the hours following the impact (Gulick et al., 2019). The increasing proportions of impact melts mixed with clasts of the target rocks in rocks below ~706 mbsf in Units 2 and 3 are interpreted to indicate that this material was emplaced prior during the initial resurge and underwent explosive interactions between melt and seawater (Gulick et al., 2019; Osinski et al., 2020; Schulte et al., 2021). Unit 3 is dominated by impact melt with poor clast abundance, demarking an approximate limit to the depth of the explosive interaction. The abundance of clays, zeolites, and other secondary alteration products throughout both units indicates persistent hydrothermal alteration (Kring et al., 2020; Simpson et al., 2020) that is particularly severe in a porous section between ~689 and 706 mbsf.

Unit 4 (747.02 mbsf to 1334.7 mbsf) includes highly damaged and displaced original target felsic magmatic rock (Zhao et al., 2020) containing occasional doleritic dikes that were bisected by zones of breccia and melt dikes during the impact event. Riller et al. (2018) document the types and abundances of different scales of mechanical disruption including intragranular and intergranular tension microcracks, mm to cm thick cataclasites, and hundreds of shear faults with decametric slip displacements all contributing to high porosities and low *P*-wave velocities. The microcrack porosity is preferentially oriented at 45° to the principal stress axis during shock (Rae et al., 2019). Detailed investigation of shock induced planar deformation features in quartz grains from the felsic protolith indicate that this material reached shock pressures of 18–20 GPa (Feignon et al., 2020). This zone, too, displays evidence of hydrothermal alteration including intermittent dissolution of quartz that increased porosity values (Kring et al., 2020). The sonic geophysical logs and multi-sensor core logging (MSCL) density measurements (Figure 3) correlate broadly, but not universally, to these core-interpretation based lithologic intervals. Shear wave speeds $V_{S\,\log} \lesssim 1.5$ km/s cannot be well constrained with the monopole logging instrument employed due to the interference of much stronger Stoneley wave modes propagating at near the sonic velocity of the borehole fluid (e.g., Paillet & Cheng, 1991); thus, only those values exceeding 1.5 km/s are shown in Figure 3.

2.3. Expedition 364 Physical Properties

The sonic compressional log velocities through upper sections of post-impact Cenozoic sediments above 585 mbsf are consistent with depth trends seen elsewhere in shallow and primarily carbonate columns (e.g., Eberli et al., 2003; Japsen, 1998). Depths to 590 mbsf had initially been informally separated into two distinct zones from 47.5 m to 280 mbsf and 280 to 590 mbsf on the basis of average VSP transit time *P*-wave speeds of 2.285 km/s ±14 m/s and 2.567 km/s ±4 m/s, respectively (Gulick, et al., 2017d). The reason for the subtle

difference between the two zones is unknown but may result from mechanical changes resulting from the transition of biogenic opal-A to opal-CT (e.g., Guerin & Goldberg, 1996; Ishii et al., 2011; Meadows & Davies, 2009), the latter indicated by X-ray identification of significant modal proportions of α-quartz, cristobalite and tridymite in the core Section 505-585 mbsf (Gulick et al., 2017e, Table T8). This variation may alternatively be due to other changes in the rock composition as seen in the abrupt change in the natural gamma radiation log (GR) that may indicate greater concentrations of clay minerals above 275 mbsl (Gulick et al., 2017d, Figure F1). Anomalously low V_P (both log and VSP ~1.800 km/s) exist at ~230–280 mbsf and this zone was likely subject to karstification as suggested by the appearance of large ~10 cm diameter vugs in the ultrasonic televiewer images.

Density ρ_{core}, V_P and V_S (both log and VSP) all rapidly increase at depths 585–617 mbsf which roughly correlates with Subunits 1E-G (Gulick et al., 2017e, Figure F43). The reasons for the increased seismic relevant properties through this interval are not explicitly known, although the gamma ray log drops at 588 mbsf, suggesting reduced clay in increased carbonate lithology. Additionally, these lowest sections of Unit 1 are also distinguished by the absence of both organic carbon (Gulick et al., 2017e, Table T6) and of opal-CT (i.e., as indicated by the lack of cristobalite and tridymite) with α-quartz being the only silica phase detected in XRD (Gulick et al., 2016; Gulick et al., 2017e, Table T8). The opal-CT to $\alpha-$quartz transition has been linked to changes in mechanical properties (Nobes et al., 1992) that have provided elsewhere sufficient material contrasts that result in clear seismic reflections (Ireland et al., 2010). In addition, the bottommost section of the post impact sediments was most certainly exposed to higher temperature hydrothermal fluid venting for at least 2.1 Myr after the impact (Kring et al., 2020). Stylolites are noted throughout Subunits 1E–G, with the highest concentration toward the bottom of this sequence in Subunit 1F (Goderis, 2019; Gulick et al., 2017e). The stylolites suggest increased compaction as a contributing factor to elevated ρ_{core}, V_P and V_S (both log and VSP) at these depths, as well. Regardless of the origin, we refer to this ~35 m thick zone (582–617 mbsf) of post impact hardened sediments as a seismic 'LID', as the contrast in its bounding seismic properties contributes significantly to the observed seismic reflection signature over the peak ring (Figure 4).

V_P, V_S (both VSP and log), and ρ_{core} all discontinuously drop across the STUC at 617.33 mbsf into Unit 2 and remain low to 705.5 m depth where increased proportions of melt rock are observed. The mechanical properties in this depth interval clearly differ (Figure 4) from that above and below and are hereafter referred to as the low velocity zone (LVZ). Unit 2 is suevite that is highly porous ($\Phi_{\text{core}} \sim = 0.2$–$0.4$), with low wave speeds observed in discrete sample measurements and the sonic log, similar to observations of suevite at the Ries Crater, Germany (Heap et al., 2020) and the Bosumtwi Structure, Ghana (Hunze & Wonik, 2007; Meillieux, 2009). In contrast to its top, the base of Unit 2 at ~722 mbsf does not correspond to any discontinuity in the mechanical properties (Figure 4). Instead, V_P, V_S (both VSP and log), and ρ_{core} increase abruptly at 705.5 mbsf in the vicinity of two thin melts near the base of Subunit 2B, and these elevated seismic properties continue through the remainder of Unit 2 and into Unit 3.

Relatively greater wavespeeds and densities (Christeson et al., 2018) persist to the bottom of the borehole through the predominantly impact melt rocks of Unit 3 (721.61–747.02 mbsf) and the highly damaged granitoids (Rae et al., 2019) with occasional dolerite, suevite, and melt dikes of Unit 4 (747.02–1334.69 mbsf; Gulick et al., 2017c). Mechanically, there is no abrupt boundary between the melt rock-rich zone commencing at 705. Five mbsf through to the base of Unit 3 with the underlying peak-ring material. However, we designate these as the seismic 'MELT' zone and the 'PR' zone due to the clear differences between their composition and suggested means of emplacement (de Graaff et al., 2021; Gulick et al., 2019; Kaskes et al., 2019).

Understanding the nature of the K-Pg reflection necessitates a close examination of the physical properties responsible for forming this event. Sharp discontinuities in the physical properties are also evident in MSCL densities (Figure 4) at the STUC and toward the bottom of Unit 2B. The lower discontinuity at 705.5 mbsf is associated with the increased presence downhole of impact melt rock and the higher values of density and wave speed continue through the melt-rock rich unit 3 (Gulick et al., 2019).

The strength of the *P*-wave seismic reflection from the contrast between two elastic media is primarily controlled by the contrasts in their *P*-wave impedance ($Z = \rho V_P$) with the normal incidence reflection coefficient *R,*

$$R = \frac{Z_2 - Z_1}{Z_2 + Z_1} \tag{1}$$

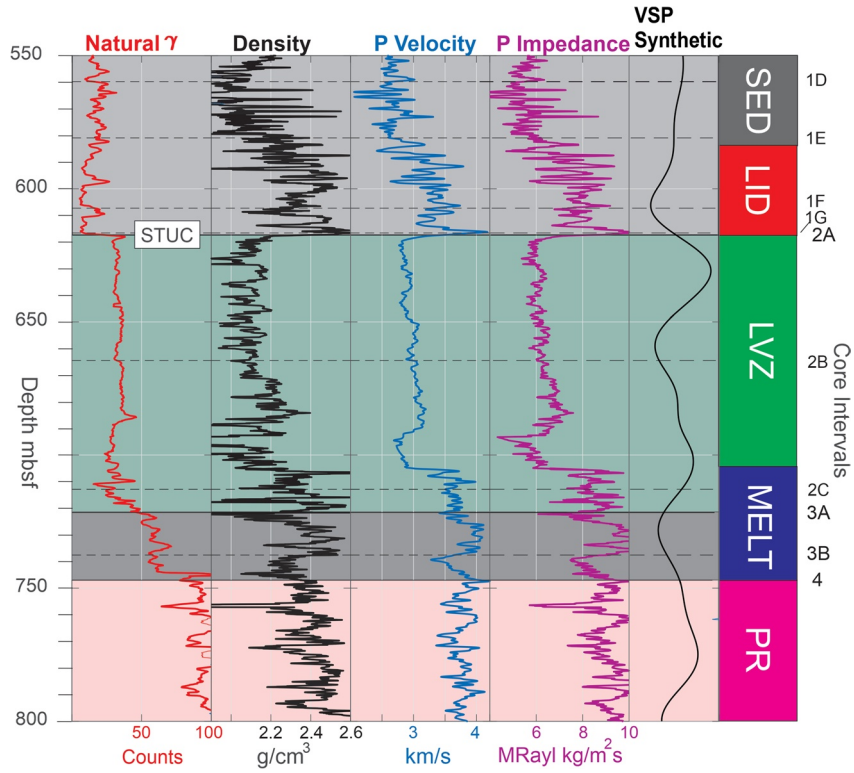

Figure 4. Details of physical properties associated with the K-Pg reflection obtained from the MSCL including the natural γ radiation, the saturated bulk density determined by γ-γ absorption, the P-wave sonic wave speeds obtained from the geophysical logs and the calculated P-wave impedance. Five mechanical zones are distinguished on the basis of changes in P-wave impedance (Z) as sediments (SED), hardened post-impact sediments (LID), low velocity zone (LVZ), melt rich zone (MELT), and displaced peak ring material (PR). The depths of the tops of the geologic intervals and subintervals interpreted from the core are denoted on the right. Discrete data points have been averaged into a continuous function with a filter radius of 5 sampling points.

where the subscripts 1 and 2 refer to the upper and lower media, respectively. Examination of Figure 4 suggests that the two impedance discontinuities at the STUC at 617.33 mbsf and within unit 2B (705.5 mbsf) which bound the LVZ would, at seismic frequencies, have large reflection coefficients of about −0.2 and +0.2, respectively. This is a key point, as large reflections originate from these impedance discontinuities and the strong reflection event is associated with the tuned superposition of these two reflections. Consequently, it is expected that the impedance architecture of this LVZ sandwiched between the earliest Cenozoic sedimentary LID and the melt rock rich zone commencing in unit 2B will strongly influence the character of the overall seismic reflection package associated with the STUC (Figure 2b).

3. Methods

3.1. Downhole Sonic Logs

The downhole sonic logs were acquired in open hole conditions with a QL40-FWS (Full Waveform Sonic, ALT/Mount Sopris Instruments) slimline tool. The tool was combined into tool strings and centered with two centralizers (see Morgan et al. (2017) for additional details). The source frequency was 6 kHz (wavelength of ~50 cm at 3 km/s). Data were acquired running uphole at 5-cm spacing. The first arrival signal was checked on the way down in the steel pipe to confirm a P-wave velocity typical of steel (5.40 km/s). The measured velocity was 5.55 km/s; thus, formation velocities may be slightly overestimated (by <3%). Data were subsequently processed with the ALT WellCAD software to calculate the compressional and shear velocities used in this work. Due to the good data quality, waveform picking was done automatically with the semblance analysis module performed on 3 receivers (R1, R2, R4), the velocity signal thus being integrated over a 0.8 m thick interval. The compressional velocities look accurate, correlating well with the discrete P-wave measurements on samples and with the

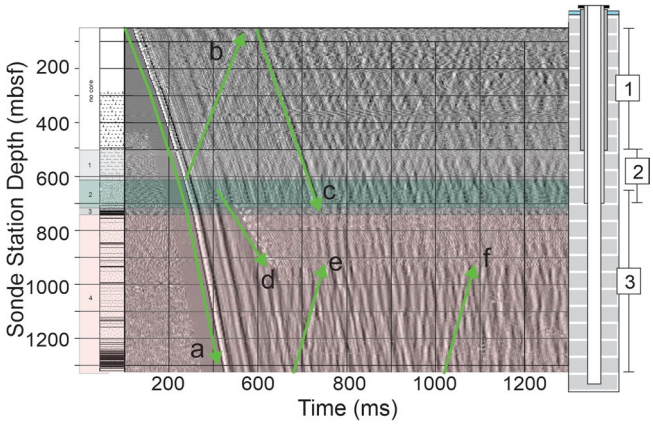

Figure 5. Raw vertical component VSP record (first peak normalization and 100 ms automatic gain control) acquired in three stages in rightmost panel (1: 47.5 mbsf – 498.75 mbsf @ 1.25 m/station, 2: 500 mbsf – 696.25 mbsf @ 2.5 m/station, 3: 652.5–1325.0 mbsf @ 5 m/station). The various arrivals a – f delineated by upward and downward arrows are described in the text.

P-wave velocity calculated from the Standard Threshold Pickup Algorithm module using the R1 and R2 receivers (spacing = 20 cm). Vs_{log} signal was not always clear and should be used with care especially in the post-impact carbonates. Down-hole depths were calculated from wireline distance and have been corrected to mbsf for consistency.

3.2. VSP Acquisition During Expedition 364 and Raw Profiles

Details of the VSP acquisition during Expedition 364 may be found in Gulick et al. (2017b), and a summary of VSP theory and methodology are provided in the supplementary information and in https://doi.org/10.7939/DVN/D1YY4A (Nixon, 2021). In brief, the 3-C records were obtained using wall-locking geophone sondes activated by an airgun source offset a few meters from the borehole. Acquisitions occurred in three separate deployments (Figure 5) because of drilling operations. The raw vertical component VSP (Figure 5) displays numerous events, including the down-going pulse (a), a strong upward-going primary reflection from the vicinity of the STUC (b), and its corresponding down-going water-surface multiple (c), as well as indications of deeper reflected events that appear to originate within the peak ring (e,f). Fortunately, tube waves (d), which can overwhelm the desired signals, only occurred over a limited depth range during stage 3 acquisition and did not seriously complicate the processing.

One key motivation for obtaining VSP data is that through appropriate processing the down-going wavefield (primarily the strong pulse wavelet) may be separated from the weaker up-going reflections (e.g., Hardage, 1985; Hinds et al., 1996) allowing the true depth of such events to be directly linked to the travel-time in the surface seismic reflection data. The up-going wavefields (Figure 6), the processing details of which are given in Text S2 in Supporting Information S1, indicate that the upward going K-Pg reflection package is a ~100 ms long event commencing with the higher impedance limestone immediately overlying the STUC at 617 mbsf.

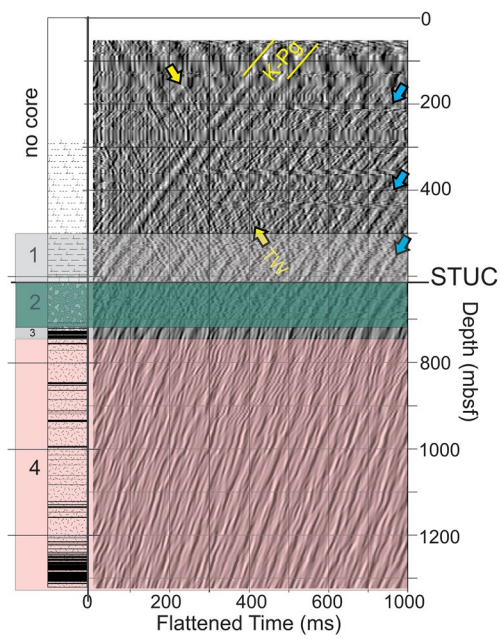

Figure 6. Separated upward-going wavefield obtained after wavefield separation compared against lithostratigraphy and four major units as interpreted from core. K-Pg boundary shown both in depth at 617 mbsf and in time. Smaller amplitude down-going tube waves are apparent with one example highlighted by yellow arrows and indicated as TW; these cannot be removed using the median filter. Upward-going events that originate beneath the K-Pg boundary are indicated by blue arrows. Wavefield characters differ above and below the top of the peak ring.

3.3. Analysis of Horizontal Components

In marine settings, zero-offset VSP data are rarely used to study *S*-waves primarily because of the difficulties associated with directly generating a shear wave using airgun sources in water where, at best, only weak *P-SV* conversions are expected. The horizontal radial and tangential polarized geophone signatures (Text S4 in Supporting Information S1) in our study are of lower amplitude than the vertical component, as expected, although they do display an *S*-wave arrival due to its polarization transverse to the borehole axis. At each depth, the horizontal components were rotated into a principal polarization direction (details on processing in Supplementary Material) yielding separate profiles for zones mostly above and below the STUC (Figure 7). The *S*-wave arrival is enhanced using polarization filtering (Montalbetti & Kanasewich, 1970). As with the vertical component wavefield, the *S*-waves observed in the upper sections of post-impact sediments (Figure 7a) show relatively continuous coherent arrivals which differ significantly from the chaotic pattern within the peak-ring (Figure 7b).

3.4. Determination of Wave Speeds

Large receiver spacings in traditional VSP experiments have limited the resolution for the determination of in situ seismic wave speeds because significant errors arise from the uncertainties associated with picking consistent

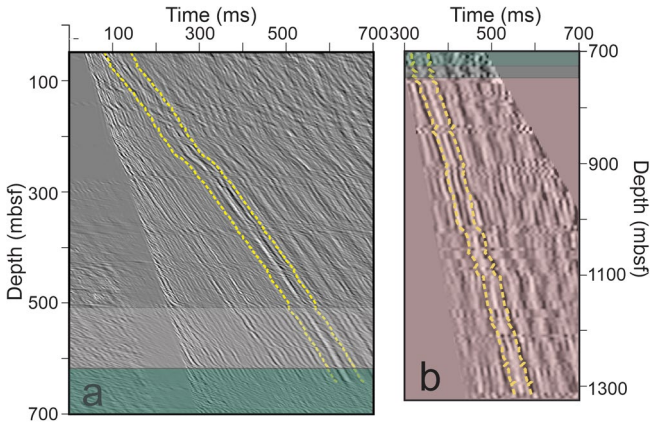

Figure 7. Optimization of Shear Wave Arrivals: Maximally rotated horizontal component profiles through (a) top of suevite (Interval 2) and post K-Pg sediments, and (b) bottom of suevite (Interval 2) through Interval 3 (melt) and Interval 4 (peak ring). Yellow lines bound the polarization analysis time window around converted S-wave. Color overlays indicate intervals as in Figure 6.

arrival times of the down-going waves for the relatively small delays between receivers. Authors have attempted to overcome this limitation by inverting their sets of observed one-way transit times to depth in VSP studies (e.g., Stephen & Harding, 1983; Stewart, 1984).

One significant difference of our data is that the wavefield was sampled at relatively close spacing, as small as 1.25 m along the borehole; this spacing allows use of a more direct 'local slope' method (Schmitt et al., 2007), which provides the in situ interval velocity together with a measure of its uncertainty. This method simply relies on equating the 'local' slope $\Delta z/\Delta t$ to the velocity via linear least squares regression of a sequence of adjacent observed one-way VSP transit times versus their depth. The square root of the variance of this slope provides a measure of the uncertainty, the expressions for which may be found in many linear regression texts (e.g., Altman & Krzywinski, 2015) and are shown within 95% certainty envelopes (Figure 8).

The P-wave arrival time used in this analysis is declared to be that of the first amplitude extremum, a negative amplitude trough of the initial direct down-going pulse. This trough is chosen to avoid complications to the pulse character introduced by interference of the primary pulse with pursuant water surface multiples and ambiguities arising from both the errors and physical meaning of picking the first detectable onset of the wave (Molyneux & Schmitt, 2000). Similarly, the *S*-wave first arrival time was chosen as the first coherent negative amplitude extremum. Unfortunately, there was not an unambiguous and coherent S-waveform in the region 640–755 mbsf and due to local slope method's sampling radius, $V_{S\,VSP}$ estimates are not available in the interval 633.75–780 mbsf. The uncertainties in $V_{P\,VSP}$ throughout and $V_{S\,VSP}$ at depths 72–628 mbsf (within the Cenozoic section) are determined with reasonable accuracy. In contrast, the 95% envelope for $V_{S\,VSP}$ at depths >780 mbsf (within the peak ring) is wide, indicating the unreliability in picking an appropriate S-wave transit time through this zone, as suggested by the complicated structure to the horizontal seismic wavefield (Figure 7b). The character of the reflection package arising from the vicinity of the STUC is analyzed by calculating 1-D 'synthetic' normal incidence reflection traces by convolving a representative wavelet with an estimated reflectivity time series (e.g., Ganley, 1981). Two different candidate wavelets were used in this basic modeling (see insets to Figures 9d and 9e). The first (Figure 9d) is obtained from the estimate of the down-going seismic wavefield directly from the VSP (See Figure S2.b in Supporting Information S1). The second is averaged from the wavelet extracted from the nearest 11 seismic traces from migrated reflection profiles CHIX17b, CHIX10, and CHIXR3 using the standard minimum phase wavelet assumption (Kanasewich, 1974). The reflectivity sequence (Figure 9i) is calculated from the observed $V_{P\,log}$ and ρ_{core} from core sampling using a recursive invariant embedding scheme (Kennett, 1974) that includes multiple reflections.

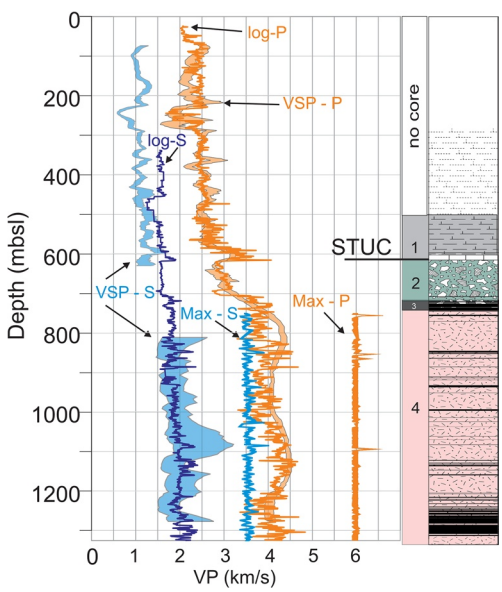

Figure 8. Observed wave speeds determined from the VSP P-wave (orange shaded trend) and S-wave (blue shaded trend) arrival times, log-P and log-S speeds interpreted from the full sonic waveforms, and intrinsic Max-P and Max-S speeds estimated for the undamaged rock on the basis of mineral modes within Voigt-Reuss-Hill bounds.

4. Results

4.1. VSP and log Derived Wave Speeds

The envelopes of the updated VSP derived compressional ($V_{P\,VSP}$) and new shear ($V_{S\,VSP}$) wave velocities (Figure 8) mostly track their corresponding sonic log values. The $V_{S\,VSP}$ are often <1.5 km/s, further reinforcing the difficulties in finding $V_{S\,log}$ from the sonic logs in these zones as mentioned earlier (Figure 3). The $V_{P\,VSP}$ increases gradually throughout the Cenozoic sedimentary carbonates aside for a low velocity excursion near 250 mbsf. Both the $V_{P\,VSP}$ and $V_{P\,log}$ show an abrupt drop in speeds at the top of the STUC below the high-velocity LID. The lower contact of the STUC is smoothed, perhaps in

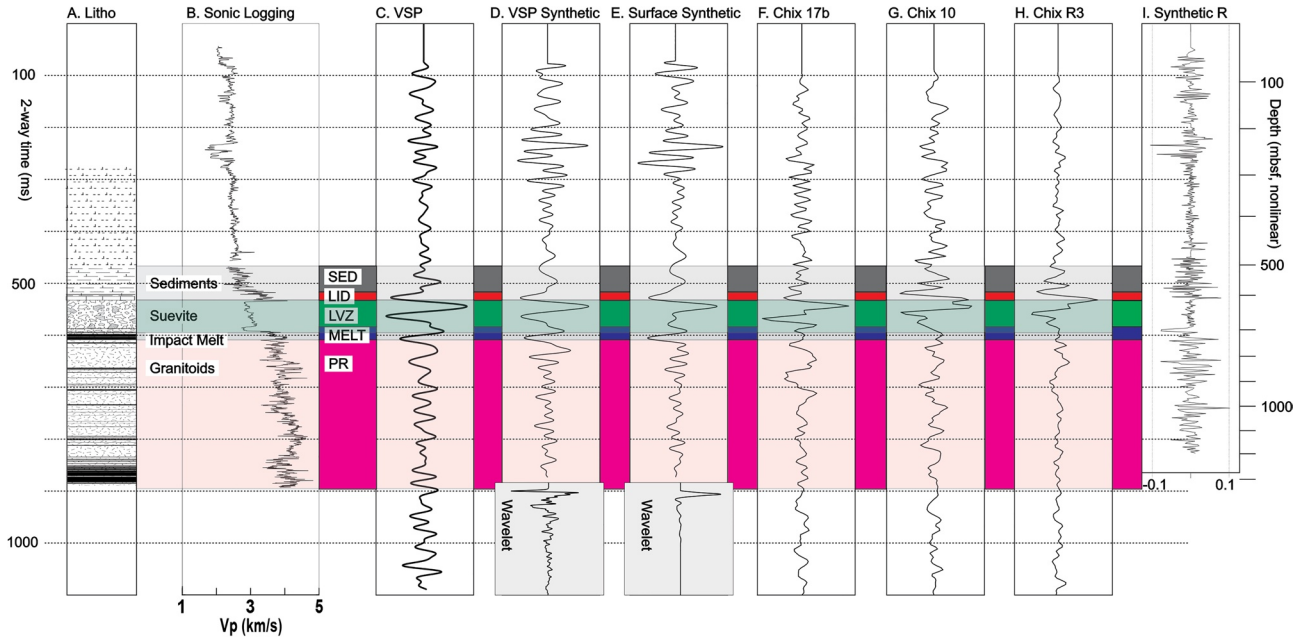

Figure 9. Observed and modeled seismic reflection responses with mechanical seismic zones (between panels) and major lithostratigraphic units (within panels). (a) Reference Lithology, (b) Sonic logging P-wave velocities, (c) Final processed VSP trace with corridor stack to mimic normal incidence reflection record, (d) Synthetic normal incidence trace from estimate of downgoing wavelet (bottom) from VSP, (e) Synthetic normal incidence trace from average estimate of wavelet extracted from migrated lines CHIX17b, CHIX10, CHIXR3 (f,g) average of 5 nearest migrated seismic traces from profiles CHIX17b, CHIX10, and CHIXR3, respectively. Correlation coefficients between various traces are shown in the supplementary methods (table S4 in Supporting Information S1).

part due to the larger spacings between the sondes (2.5 m) in the depth interval 500–696.25 mbsf, compared to a spacing of 1.25 m at depths 47.5–498.75 mbsf.

4.2. Intrinsic Wave Speeds of Undamaged Peak Ring Materials

The deficit in both the sonic logging and $V_{P\ VSP}$ relative to the expected lithologies within the peak ring has already been noted (Christeson et al., 2018) and attributed primarily to the damage-induced porosity. The $V_{S\ log}$ and the more poorly constrained $V_{S\ VSP}$ measures described here, too, are significantly below the speeds expected for the target granitoids. We quantify this deficit more fully by calculating the speeds expected for the undamaged mineral crystallite (granite) of the peak ring materials on the basis of the mineral volumetric modal fractions $\varphi_i(z)$ and the corresponding intrinsic isotropic moduli K_i and μ_I (Table 1). The constituent mineral phases from the X-ray diffraction core analyses reported in Gulick et al. (2017c, Table T5) and Gulick et al. (2017c, Table T4) are used to first calculate the undamaged bulk rock $K_o(z)$ and shear $\mu_o(z)$. The upper Voigt K_V and μ_V and lower Reuss K_R and μ_R bounds constrain the allowable values of $K_o(z)$ and $\mu_o(z)$ with

$$K_V(z) = \sum \phi_i(z) K_i \geq K_o(z) \geq \left[\sum \frac{\phi_i(z)}{K_i}\right]^{-1} = K_R(z) \quad (2)$$

And

Table 1
Isotropic Elastic Moduli and Density for Primary Constituent Minerals in Peak Ring (Bass, 1995)

Mineral	Quartz	Albite	Microcline	Sanidine	Orthoclase	Anorthite	Augite
ρ (kg/m^3)	2648	2610	2567	2520	2571	2765	3320
K (GPa)	37.8	56.9	55.4	58.8	62	84.2	95
μ (GPa)	44.3	28.6	28.1	30.1	29.3	39.9	59

$$\mu_V(z) = \sum \phi_i(z)\mu_i\phi_i(z)\mu_i \geq \mu_o(z) \geq \left[\sum \frac{\phi_i(z)}{\mu_i}\right]^{-1} = \mu_R(z) \tag{3}$$

Hill (1952) suggested that the simple average of these bounds provided an adequate estimate, but we retain both Voigt-Reuss-Hill (VRH) bounds. The bounds for the wavespeeds expected for the nonporous and undamaged rocks are then

$$\sqrt{\frac{K_V(z)+4\mu_V(z)/3}{\rho_o(z)}} = \sqrt{\frac{M_V(z)}{\rho_o(z)}} \geq V_{Po}(z) \geq \sqrt{\frac{K_R(z)+4\mu_R(z)/3}{\rho_o(z)}} = \sqrt{\frac{M_R(z)}{\rho_o(z)}} \tag{4}$$

where M is the longitudinal, or P-wave, modulus, and

$$\sqrt{\frac{\mu_V(z)}{\rho_o(z)}} \geq V_{So}(z) \geq \sqrt{\frac{\mu_R(z)}{\rho_o(z)}} \tag{5}$$

where the pore-free rock intrinsic density is

$$\rho_o(z) = \sum \phi_i(z)\rho_i \tag{6}$$

The VRH bounded $V_{P\,VRH}$ and $V_{S\,VRH}$ are shown in Figure 8 and are the estimates for the unaltered isotropic polycrystalline rock, with no attempt to incorporate pores or microcracks. The values will be in error within the melt rock zones as neither the volume fractions of melt rock nor the glass moduli are well constrained. The observed VSP compressional wavespeeds within the peak ring (~4–4.5 km/s) are only about 65%–75% of the VRH bounds (~6 km/s), illustrating the large deficits in wave speeds caused by shock induced damage and fracturing/faulting during peak ring formation.

The stack of the final VSP corridor (see processing details Figure S2e in Supporting Information S1) produces a seismic reflection trace in two-way time (Figure 9c) that is compared against the neighboring seismic reflection profiles CHIX10, CHIX17b, and CHIXR3 located at distances from the borehole of approximately 160 m, 200 m, and 350 m, respectively. With these offsets of the seismic profiles to the borehole we cannot expect the trace to match perfectly, with a correlation coefficient of 0.4068 between the real VSP trace and nearest profile CHIX10 (Table S4 in Supporting Information S1). The strong reflection just below 600 m depth (Figures 9, Figure 6) is the event originally interpreted to be the top of the K-Pg boundary section within the crater. However, the character of this event is not one of a simple primary reflection. As noted, the velocity structure near the STUC consists of rapidly increasing wavespeeds with depth in the Cenozoic sedimentary carbonates of the LID with a sharp decrease into the highly altered underlying suevites of the LVZ followed at ~700 m by a second abrupt increase at the top of the unsorted melt rich suevites, coinciding with the LFR.

The synthetic VSP trace (Figure 9d) captures well the character of the observed VSP trace (Figure 9c), confirming that the reflection package originates from interference of reflections from the complex impedance structure both above and below the STUC (Figure 4). The synthetic calculated using the wavelet extracted from the seismic profile (Figure 9e) also captures this behavior. This extracted wavelet, however, has a broader frequency bandwidth and is sharper in the time domain; this nearly allows for separation of the events originating at the Z discontinuities top and bottom of the LVZ.

5. Discussion

5.1. Nature of the K-Pg Reflection Event

The characteristics of the upward-going wavefields differ significantly above and below the STUC (Figure 6). No upward traveling coherent events that could be interpreted as a seismic reflection are apparent in the wavefield within the peak ring granitoids. This contrasts with the continuous events, even those that must originate within the peak ring (with a few indicated by blue arrows, Figure 6), that characterize the wavefield above the STUC. These coherent reflections originating from the granitoids may originate from fault planes within the peak ring (Morgan et al., 2016); however, they do not stack well during processing of the surface seismic profile

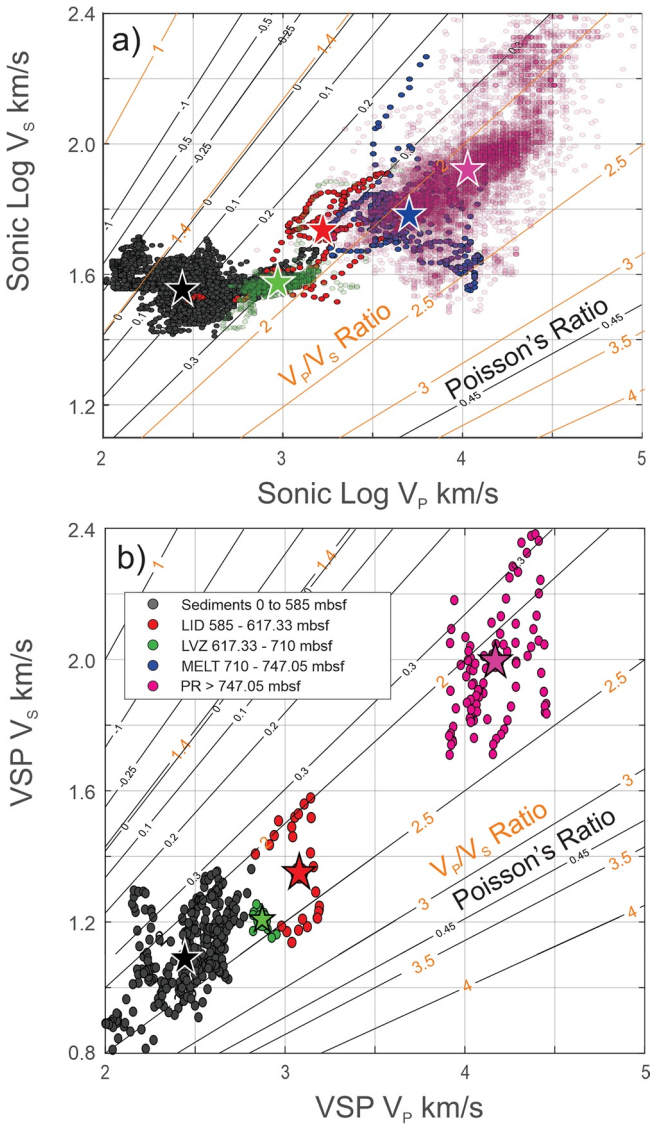

Figure 10. V_P vs. V_S cross-plots with lithologic mechanical lithologies demarcated by colored symbols superimposed on Poisson's ratio and V_P/V_S ratio contours for (a) the sonic log and (b) the VSP analysis. $V_{s\,VSP}$ data unavailable for the MELT. Average values for each lithology are denoted by stars.

into continuous coherent events, suggesting that the lateral dimensions of the heterogeneity within the peak ring materials may not be larger than the Fresnel zone of the 2005 multichannel seismic data (~500 m width).

Curiously, there is no evidence for the *LFR* seen in the surface profiles throughout at least the full 3 s of the VSP record (not shown), even after applying numerous bandpass filters that would enhance lower frequency arrivals. This absence may mean that the conditions necessary to produce the LFR may not exist at the borehole location. Differences in the thickness of the MELT zone away from the drill site, for example, might explain the reflector. Alternatively, one cannot discount the possibility that this LFR could instead be due to reflections originating out of the plane of Line CHIX10 from the rugose 3D topography of the peak ring; the LFR may not result from in-plane physical property contrasts. This issue could only be resolved by conducting a high-resolution 3D seismic program.

Hydrothermal fluids have altered the mechanical properties and possibly the density of the original impactites and early post-impact sediments. As a result, the local character of the K-Pg seismic event may depend on the duration, fluid fluxes, temperatures, and compositions resulting from the hydrothermal cooling after the impact. Much of the area will have been covered with the impactites which were then subsequently buried by continued sedimentary deposition; however, the mechanical character of these deposits may depend strongly on the persistent hydrothermal flux. In cooler regions with less fluid flow, such a distinct seismic LID may not have formed and the sharp *Z* discontinuity at the STUC (Figure 4) may not have developed. Many of the rock layers immediately overlying Unit 1D have higher clay content, which may partly explain the rapid change in wave speeds. The increasing V_P (both log and VSP) in these layers is accompanied by a trend of diminishing porosity; the reasons for this are unknown, but this may be related to precipitation of minerals brought up by the vigorous hydrothermal circulation that occurred for at least 2 Myr post impact (Kring et al., 2020) or by variations in the compaction.

5.2. Relationships of Velocities

Although a rock mass' elastic moduli and density contain more fundamental information about a material, often all that can remotely be observed are V_P and V_S, and the spatial distribution of these can self-consistently define structure.

Presented here are values of both V_P and V_S measured by moderate frequency sonic logs (6 kHz, Figure 10a) and seismic VSP frequencies (~100 Hz, Figure 10b). Additional insight may be gained from the simple $R = V_P/V_S$ ratio or the closely related dynamic Poisson's ratio ν that for an isotropic material is:

$$\nu = \frac{1}{2}\frac{R^2 - 2}{R^2 - 1} \tag{7}$$

In isotropic materials, $-1 \le \nu \le 0.5$ is theoretically allowed, although for rocks the range $0 \le \nu \le 0.5$ ($R \ge \sqrt{2}$) is more realistic. Negative apparent ν can appear if anisotropy is not appropriately considered (Wang et al., 2012).

R or ν has been used in numerous studies to augment the interpretation of observed V_P and V_S, which are nonunique by themselves, over the range of scales from the lithosphere (e.g., Golos et al., 2020) to the near surface. It is useful to review what trends might be expected. For example, in the case of pore-free crystalline igneous rocks, ν can often provide some indication of mineralogical content; ν is particularly useful with respect to quartz, which

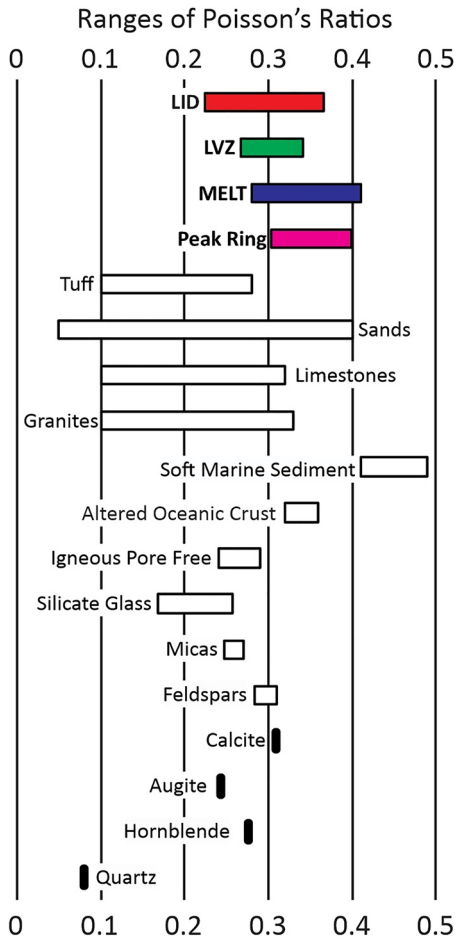

Figure 11. Poisson's ratio for various lithologies contrasted with those observed in the Chicxulub borehole.

has an anomalously low ν near 0.06 (e.g., Christensen, 1996). In porous sediments, ν is sensitive to different factors which include mineralogy, porosity, pore geometry, effective confining stress, pressure, temperature, and saturation state (Hamilton, 1979). Modeling of the effects of crack densities on elastic properties using available theories show that R generally increases with crack density (e.g., Dunn & Ledbetter, 1995; O'Connell & Budiansky, 1974). Additionally, ν is important in controlling the reflection amplitudes' dependence on angle of incidence, thus ν is routinely sought during inversion of common midpoint active source seismic profiling (e.g., Li and Zhao, 2014).

Figure 11 compares the ν values observed here separately for the LID, the LVZ, the MELT, and the peak ring material against similar terrestrial rocks and their constituent minerals. The mineral values are the Hill averages calculated for isotropic monocrystalline crystallites; aside from the anomaly of quartz, most of the minerals will have ν of 0.25–0.3. The values of ν for pore free silicate glasses with felsic to mafic compositions increase from 0.168 to 0.257 as the SiO_2 content decreases (Meister et al., 1980). Poisson's ratios for pore free igneous rocks fall within a relatively small range, but the presence of micro-cracks that are open at lower confining pressures strongly influences the material moduli and allow for a much wider range of ν as indicated for granite. Limestones and sandstones have large ranges of observed ν which are dependent upon the wide range of porosities and compositions encountered. Loosely consolidated siliciclastic sediments, primarily muds and sands, are not expected at depth at the drill site; however, they are shown as they illustrate materials with vanishing rigidity.

The ranges for the LID, LVZ, MELT, and PR in Figure 11 encompass 95% (mean $\pm$ 2 standard deviations) of the calculated ν (Equation 7) from the velocity observations at all depths in each interval (Figure 10). The primarily calcite and α-quartz bearing LID sediments fall within ranges comparable to low porosity limestones with the mean ν below that for pure calcite. The ν for the post-impact LID sediments is at the high end of that expected for carbonates, and the mean value is close to that for a monocrystalline calcite crystallite. These values are not atypical for low porosity carbonates (e.g., Njiekak & Schmitt, 2019). The ν for the LVZ (Figure 12), MELT, and peak ring (Figure 11) are all anomalously high relative to the closest comparable terrestrial lithologies of tuffs and the constituent silicate melts. Only low velocity oceanic mafic materials, that have also experienced hydrothermal alteration near mid-ocean ridges, have similar values (Figure 11). The unusual ν ranges for the Chicxulub borehole rocks are likely due to an anomalously low shear modulus as a result of multiple underlying factors. The VSP shear waveform is poorly resolved in the LVZ, which further supports the assumption of an anomalously low shear modulus.

The LVZ is a fining upward breccia with a matrix primarily composed of shocked ejecta particles. However, the fining upward trend is general, and periodically reverts back to coarser grains which modulates the fining upward trend with an oscillatory character. ν and clast size both generally increase with depth within the LVZ, and major grain size discontinuities appear at roughly the same depths as discontinuities in ν (Figure 12). Although there is a correlation between the LVZ fining upward sequence and ν, this is not necessarily causative and further investigations into this trend are warranted.

5.3. Assessment of Damage in Peak Ring Materials

Numerical models of the formation of large impact structures are one key tool to understanding the evolution pressures, temperature, deformation, and final structure (Melosh et al., 1992; Okeefe & Ahrens, 1993) that have progressively evolved to incorporate increasingly sophisticated estimates of porosity or damage (Collins, 2014; Collins et al., 2004; Ivanov et al., 1997; Melosh et al., 1992; Wiggins et al., 2019). There are numerous attempts to constrain the models from morphology (e.g., Baker et al., 2016), gravitational signatures

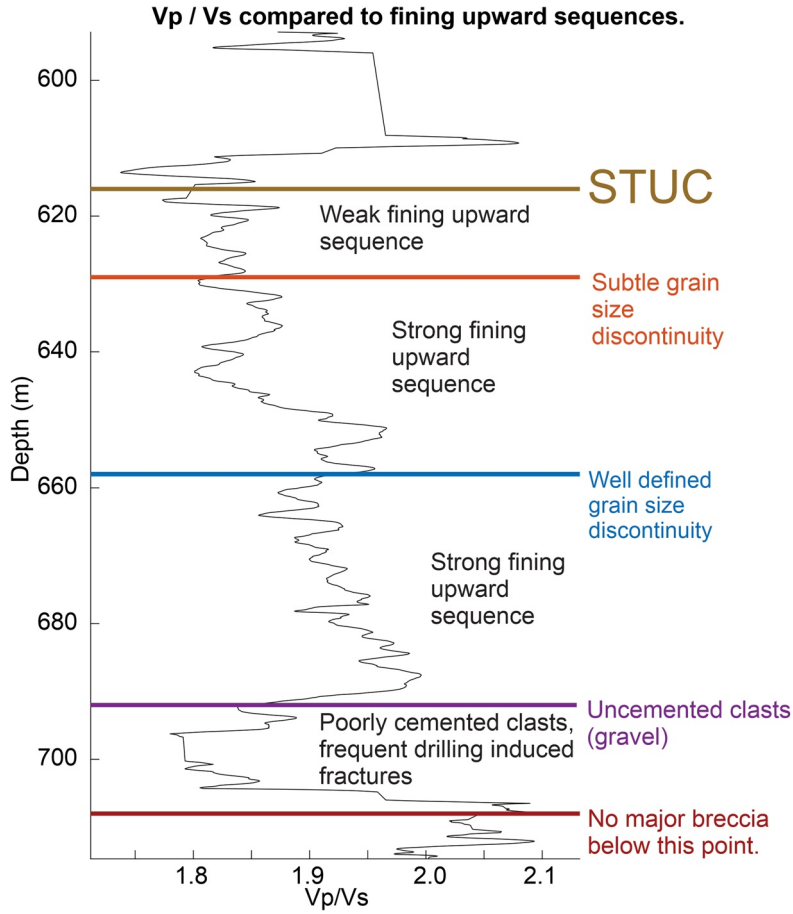

Figure 12. Vp/Vs ratio in the Suevitic LVZ.

(Pilkington & Grieve, 1992), or seismic imaging (e.g., Collins et al., 2002). However, as noted by Collins (2014), calibrating the levels of damage predicted in the models against actual impact structures remains challenging on Earth due to the paucity of available pristine impact structures and the difficulties associated with direct observation through drilling. Mapping of the structures in terms of seismic wave speeds that are sensitive to damaged porosity can potentially provide some additional constraints.

In terrestrial situations, the influence of abundant macroscopic fractures and microcracks in diminishing seismic wave speeds or elastic moduli as manifest by their nonlinear stress dependence has been known for over a century (Adams & Williamson, 1923). The rock engineering community has most directly sought to exploit this link via empirical relationships between P-wave velocities and various measures of rock damage such as the rock quality index (Boadu, 1998; Dickmann, 2020; Sjogren et al., 1979). At larger scales, various lines of evidence including trapped modes (e.g., Gulley et al., 2017), seismic tomography (e.g., Cochran et al., 2009; Thurber, 2006), and interferometry of ambient noise (e.g., Brenguier et al., 2019) suggest zones of diminished seismic velocities that are interpreted as high levels of damage near fault zones in the brittle upper-crust (Ben-Zion & Sammis, 2003; Caine et al., 1996). Measurements from boreholes using sonic logs (Moos & Zoback, 1983; Stierman & Kovach, 1979), cross-well measurements (e.g.,Wong et al., 1983), and near surface refraction (Rempe et al., 2013) also indicate the fracturing significantly lowers the waves speeds relative to laboratory measurements on the intact materials. Generally, both V_P and V_S are reduced in such zones translating to increased R and ν. Efforts have attempted to extract the degree of damage from the observed wave speeds (e.g., Benson et al., 2006; Schubnel et al., 2006). However, the correlations may not always be as direct as hoped (Rempe et al., 2018; Swanson et al., 2020).

In developing a model of the dynamic fragmentation of materials that is employed in many impact models, Grady and Kipp (1987) defined the scalar measure of damage D that is bounded between 0 and 1. These bounds indicate the evolution from a fully intact undamaged material (value of 0) to a state of complete failure and disaggregation

(value of 1), such that it cannot support a tensile stress. As such, D is intended to be an internal state variable that indicates the intensity of fracture damage in the material and is quantified through the reduction of the material's flaw-free elastic modulus B_o to that for the given level of damage $B = (1 - D)B_o$. However, Grady and Kipp (1987) did not specify which elastic modulus should be used. Bearing this concern in mind and using the simple relation $B = \rho(V_B)^2$, Ahrens and Rubin (1993) expressed D in terms of either V_P or V_S corresponding to the damaged longitudinal (P-wave) $M_d = K_d + 4\mu_d/3$ and shear μ_d moduli, respectively as

$$D_P = 1 - \frac{M_d}{M_o} = 1 - \frac{\rho}{\rho_o}\left(\frac{V_P}{V_{Po}}\right)^2 \tag{8}$$

And

$$D_S = 1 - \frac{\mu_d}{\mu_o} = 1 - \frac{\rho}{\rho_o}\left(\frac{V_S}{V_{So}}\right)^2 \tag{9}$$

One could also describe a damage parameter D_K using knowledge of the damaged K_d and intrinsic K_o bulk moduli less directly:

$$D_K = 1 - \frac{K_d}{K_o} = 1 - \frac{\rho}{\rho_o}\left[\left(\frac{V_P}{V_{Po}}\right)^2 - \frac{4}{3}\left(\frac{V_S}{V_{So}}\right)^2\right] \tag{10}$$

Ahrens and Rubin (1993) simplified Equations 8 and 9 by assuming that $\rho \approx \rho_o$, but we retain these terms given the large observed differences here and because damaged ρ are available from the core.

The damage parameters have been used in numerous high-velocity impact laboratory studies to assess the degree of material disruption. D_P and D_S have been particularly useful metrics to track changes in the degree of disruption extending radially from impacts into large target blocks. This is accomplished by measuring V_P directly on samples cut from the shocked blocks (Ahrens & Rubin, 1993; Ai & Ahrens, 2007) or indirectly via wave speed tomography (Moser et al., 2013; Raith et al., 2018; Xia & Ahrens, 2001). D_P has been particularly useful in connecting damage to attenuation and induced micro-crack densities (Liu & Ahrens, 1997) in materials from these experiments, although these the magnitudes of these damage measures were not linked more directly to levels of strain experienced by the sample. Further, we are not aware of any prior damage parameters estimates from rock samples or indirect seismic measurements on terrestrial impact structures.

The in situ seismic wavespeeds in hole M0077a are highly attenuating, as shown by low Q factors (Figure 13d) from spectral ratio analysis (Nixon et al., 2020). Curiously, although attenuation decreases with depth within this hole as shown by increasing Q, damage parameters appear to be relatively consistent throughout the hole (Figure 13b). The values shown in Figure 13b all indicate high levels of damage within the peak ring materials, yet the values of the three damage parameters differ significantly from one another. D_S is always larger (0.7–0.75) than D_P (0.5–0.6), with D_k laying between the two values, by definition of elastic moduli. This indicates that the deficit of V_S is greater than that for V_P as was suggested by the elevated values of R. The reasons for this discrepancy are not yet understood, but may be related to the displaced materials' point of origin within the un-displaced target hemisphere. Wiggins et al. (2019) incorporated tensile and shear damage parameterization into shock physics hydrocode iSALE-2D for hypervelocity impacts from 100 m to 100 km in diameter in Lunar basalt; both tensile and shear damage with similar values to those shown here (~0.5 and 0.75, respectively) were found on the boundary between the pure shear damage zone and mixed shear/tensile damage zone, at ~1/10 of the radius of the transient crater.

5.4. Characterization of Block Sizes

Within the PR, $V_{P\,log}$ (λ ~1m) are ~5% less than $V_{P\,VSP}$ (λ ~ 50m); this discrepancy is more pronounced in the upper PR, approaching 15% (Figure 8). With a similar trend observed in the longitudinal damage parameter (blue circles compared to solid blue lines in Figure 13), this frequency dependent response may be due to dominance of characteristic acoustic fluidization block size (Riller et al., 2018). Riller et al. (2018) suggest a characteristic block size as low as 2.3 m, on the basis of cataclasite and ultra cataclasite zones. This finding is supported by a relatively high cataclasite count in the region 750 mbsf – 850 mbsf, the depth with the greatest sonic/VSP V_P

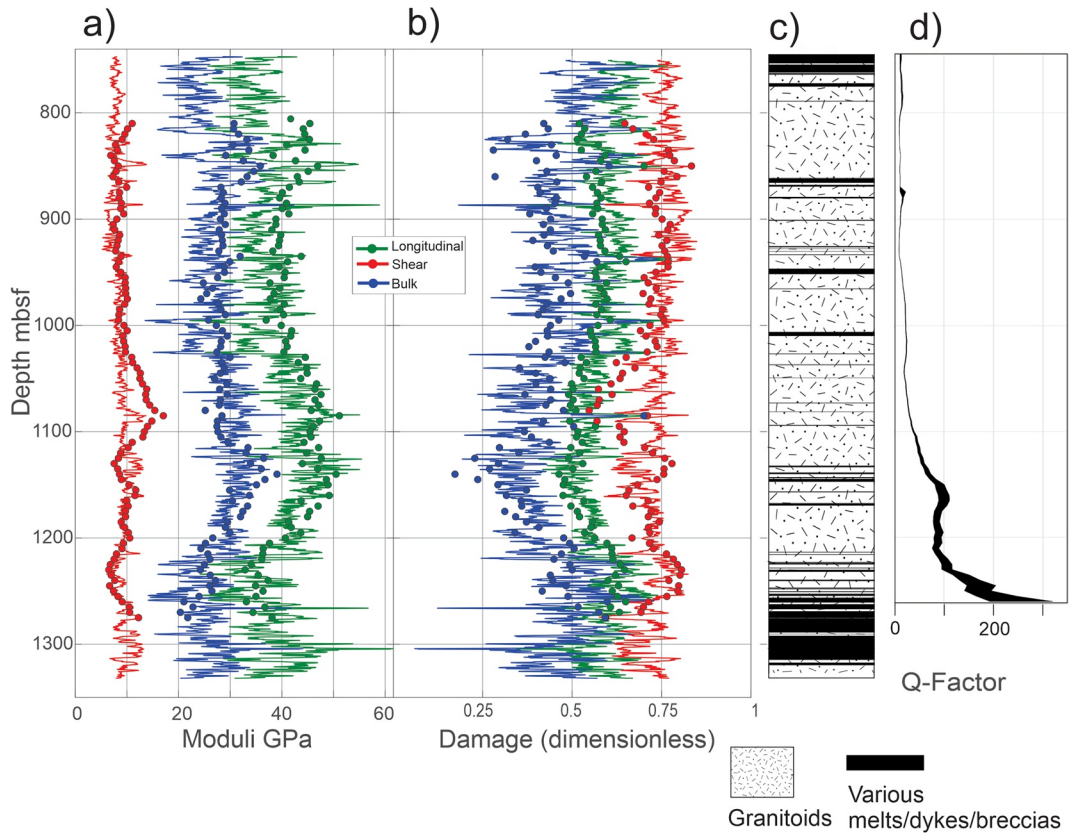

Figure 13. Damage parameterization of peak ring granitoids and simplified geological column. (a) Dynamic longitudinal or P-wave (green), bulk (blue), and shear (red) moduli. (b) Corresponding longitudinal (green), D_P bulk (blue), and shear (red) D_S damage parameters. Continuous lines calculated from sonic log velocities. Discrete filled circles calculated using VSP obtained velocities. (c) Simplified stratigraphy. (d) Quality factor versus depth, originally from Nixon et al. (2020).

discrepancy (Figure 8). However speculative, dominance of smaller effective acoustic fluidization block size toward the top of the PR granitoids is additionally confirmed intuitively, since smaller blocks would be displaced farther more easily.

5.5. Implications for Future Extraterrestrial Seismic Investigations

The gross features of the Chicxulub structure remain well preserved, owing to burial by later Cenozoic sediments. As such, it is worthwhile to consider how Chicxulub might serve as an analog to future hypothetical extraterrestrial seismic investigations on the Moon or Mars. Larger impact craters on all of these bodies will typically exhibit central peaks or peak rings, melt sheets, and breccia/suevite veneers. To reiterate, vertical seismic data at site M0077 on the peak ring of Chicxulub includes reflections originating from the discontinuities in impedance at the top and bottom of the LVZ. These contrasts may be influenced by long-term hydrological alteration of the original breccias and suevites with the fluid fluxes potentially also stiffening the sediments of the LID; much of this response relied on the abundance of water. Additionally, the presence of a sorted suevite that makes up the bulk of the LVZ (Units 2a and 2b above 705.5 mbsf) required water in the form of an ocean resurge (Gulick et al., 2019; Ormö et al., 2021).

There is abundant evidence for the existence of surface water in Mars' past from numerous lines of inquiry (Filiberto & Schwenzer, 2018), and extensive reservoirs may still reside in its subsurface (Lasue et al., 2019). The presence of abundant water, even if it originates underground, suggests that the impactites on Mars could similarly be subject to post-impact hydrological alteration. Whether the structure might be preserved by subsequent sedimentation would depend critically, as it does on Earth, on the nature and location of the target (e.g., land, liquid water, ice, etc.) and size/speed of the impactor. However, atmospheric conditions on Mars have likely not

been conducive to standing bodies of water for nearly 3.7 Ga (Pollack et al., 1987; Worsdworth, 2016), suggesting that any potential analogy between the seismic responses of a sedimentary capped Martian impact structure and the seismic structure of Chicxulub may only be relevant for pre-Noachian and Noachian impacts.

Free water is not expected in any important quantities in the Moon (Honniball et al., 2021), likely precluding any significant hydrothermal alteration of impactites after the volatile depletion period (Hauri et al., 2015) of lunar history. Older lunar impact structures, however, will be buried by the slow progressive buildup of the regolith. Controlled source seismic tests during the Apollo program suggest that V_P of the regolith near the surface is very low (Cooper et al., 1974; Kovach & Watkins, 1973). One might reasonably expect the seismic properties of the displaced and damaged 'bedrock' with the proximal blanketing by melt and breccias to be similar to those at Chicxulub described here. Consequently, although there will be no hydrothermal alteration, one could anticipate a strong contrast in seismic impedance between impactites and later deposited regolith.

Although impact structures are rare on Earth, they dominate the crusts of many other rocky bodies. Understanding damage in the near surface lithology will be important for construction projects on our own Moon, of which ~1/2 of the surface is impact ejecta and likely all has at least micrometeorite damage (Anders et al., 1973). Indeed, impact basins are flat and low in elevation, both desirable traits for lunar construction projects; understanding the geoengineering response in impact basins is therefore important for successful colonization of the Solar System.

6. Conclusions

Detailed analysis of the vertical seismic profile obtained during the IODP/ICDP Expedition 364 Chicxulub impact structure scientific drilling project reveals the factors controlling the character of the K-Pg seismic boundary reflection event, illustrates the chaotic nature of the seismic wavefield within the highly damaged peak ring, and allows for assessment of damage levels.

Modeling confirms that the character of the seismic reflections at Site M0077 within the impact sequence results primarily from tuning of reflections originating at the abrupt discontinuities in impedance at the top and bottom of a low velocity zone (LVZ) formed dominantly of suevite deposited by ocean resurge. The mechanical and density variations that control the seismic reflectivity at the top of the Chicxulub structure are clear. However, the reasons for the high seismic impedance of the earliest sedimentary materials relative to the underlying suevite and melt rock of the LVZ are not so apparent. Hydrothermal alteration has been well documented in the LVZ, and the change in mineralogy and porosity will certainly have influenced the wave speeds and density through this zone. These fluid fluxes also likely contributed to stiffening those sediments deposited following the impact forming the higher sedimentation rate portions of Paleocene section of the LID, but whether such circulation could persist long enough to explain the elevated density and wave speeds through the younger Eocene sediments is not obvious. Other mechanisms that could play a role include compaction and cementation. Additional detailed studies, including microscopy to elucidate pore structures and the prevalence of dissolution, or secondary precipitation of minerals, and mechanical wave speed and strength measurements on the core materials through the LID, particularly those above the Paleocene-Eocene Thermal Maximum that have not yet received much attention, will be necessary to better understand the factors influencing the physical properties of these sediments.

The character of the seismic wavefield changes significantly as it passes from the post-impact impactites and sediments into the highly damaged peak ring granitoids. The upgoing vertical component wavefield displays clear reflections in the sediments, whereas no strong coherent events exist within the peak ring. From the horizontal components, a weak but distinct shear wave may be followed through the sediments; however, this wavefield becomes chaotic in the peak ring, making tracing a shear arrival tenuous. These observations indicate a highly heterogeneous structure to the peak ring that scatters the seismic energy. A full understanding of this phenomenon is beyond the scope of this contribution, but efforts are underway to better characterize this through various measures such as apparent attenuation (Nixon et al., 2020).

V_s values from both sonic logging and the VSP are anomalously low within the Chicxulub peak ring, consistent with earlier studies that documented anomalously low V_P and ρ in this region. Having measures of both V_P and V_S allows determination of their ratio R and of Poisson's ratio ν, both of which are elevated relative to comparable, but undamaged, terrestrial lithologies. As such, R and ν could be useful attributes for mapping the extent of damage beneath impact structures on the terrestrial planets.

The observed velocities were further used to calculate damage parameters D_i following the definition of Grady and Kipp (1987) that have been used previously to delineate damage zones in laboratory impacts. We were able to use peak ring mineralogy and core density values to determine D_P, D_S, and D_K based respectively on the dynamic longitudinal, shear, and bulk moduli. The goal of this analysis is, as with R and ν, to provide observational constraints to assist in refining advanced numerical impact models that currently incorporate *Grady-Kipp* fragmentation concepts in calculating shock induced strain or porosity.

Data Availability Statement

The organized data used here are freely available at https://doi.org/10.7939/DVN/D1YY4A Nixon (2021).

SPSG and GLC were supported by NSF grant OCE-1737351. This is University of Texas Institute for Geophysics Contribution 3879 and Center for Planetary Systems Habitability Contribution 0049. The authors have no conflicts of interest.

Acknowledgments
The authors thank J. Melosh and B. Johnson for insight into the inclusion of strain within impact modeling codes, D. Goldberg for advice on sonic log results, and J. Morgan for suggestions on improving the manuscript. This research used samples and data provided by IODP. Samples can be requested at http://web.iodp.tamu.edu/sdrm. Expedition 364 was jointly funded by the European Consortium for Ocean Research Drilling (ECORD) and the International Continental Scientific Drilling Program, with contributions and logistical support from the Yucatán State Government and Universidad Nacional Autónoma de México (UNAM). The downhole seismic system was provided by the Canada Foundation for Innovation Leaders Opportunity Fund Grant #31419.

References

Ackermann, H. D., Godson, R. H., & Watkins, J. S. (1975). Seismic refraction technique used for subsurface investigations at Meteor Crater, Arizona. *Journal of Geophysical Research*, *80*(5), 765–775. https://doi.org/10.1029/jb080i005p00765

Adams, L. H., & Williamson, E. D. (1923). On the compressibility of minerals and rocks at high pressures. *Journal of the Franklin Institute*, *195*, 475–529. https://doi.org/10.1016/s0016-0032(23)90314-5

Ahrens, T. J., & Rubin, A. M. (1993). Impact-induced tensional failure in rock. *Journal of Geophysical Research*, *98*(E1), 1185–1203. https://doi.org/10.1029/92je02679

Ai, H. R. A., & Ahrens, T. J. (2007). Effects of shock-induced cracks on the ultrasonic velocity and attenuation in granite. *Journal of Geophysical Research*, *112*(B1), 9. https://doi.org/10.1029/2006jb004353

Altman, N., & Krzywinski, M. (2015). Points of significance: Simple linear regression. *Nature Methods*, *12*(11), 999–1000. https://doi.org/10.1038/nmeth.3627

Anders, E., Ganapathy, R., Krähenbühl, U., & Morgan, J. W. (1973). Meteoritic material on the moon. *The Moon*, *8*(1–2), 3–24. https://doi.org/10.1007/bf00562747

Angenheister, G. A. & Pohl, J. (1976). Results of seismic investigations in the Ries Crater area (southern Germany). In *Explosion seismology in central Europe*, Springer: 290–302. https://doi.org/10.1007/978-3-642-66403-8_38

Baker, D. M. H., Head, J. W., Collins, G. S., & Potter, R. W. K. (2016). The formation of peak-ring basins: Working hypotheses and path forward in using observations to constrain models of impact-basin formation. *Icarus*, *273*, 146–163. https://doi.org/10.1016/j.icarus.2015.11.033

Bass, D. J. (1995). Elasticity of minerals, glasses and melts. In T. J. Ahrens (Ed.), *Mineral physics and crystallography, Ref. Shelf ser* (Vol. 2, pp. 45–63). AGU.

Bell, C., Morgan, J., Hampson, G., & Trudgill, B. (2004). Stratigraphic and sedimentological observations from seismic data across the Chicxulub impact basin. *Meteoritics & Planetary Sciences*, *39*(7), 1089–1098. https://doi.org/10.1111/j.1945-5100.2004.tb01130.x

Benson, P., Schubnel, A., Vinciguerra, S., Trovato, C., Meredith, P., & Paul Young, R. (2006). Modeling the permeability evolution of microcracked rocks from elastic wave velocity inversion at elevated isostatic pressure. *Journal of Geophysical Research*, *111*, B4. https://doi.org/10.1029/2005jb003710

Ben-Zion, Y., & Sammis, C. G. (2003). Characterization of fault zones. *Pure and Applied Geophysics*, *160*(3), 677–715. https://doi.org/10.1007/pl00012554

Boadu, F. K. (1998). Inversion of fracture density from field seismic velocities using artificial neural networks. *Geophysics*, *63*(2), 534–545. https://doi.org/10.1190/1.1444354

Brenguier, F., Boué, P., Ben-Zion, Y., Vernon, F., Johnson, C. W., Mordret, A., et al. (2019). Train traffic as a powerful noise source for monitoring active faults with seismic interferometry. *Geophysical Research Letters*, *46*(16), 9529–9536. https://doi.org/10.1029/2019gl083438

Caine, J. S., Evans, J. P., & Forster, C. B. (1996). Fault zone architecture and permeability structure. *Geology*, *24*(11), 1025–1028. https://doi.org/10.1130/0091-7613(1996)024<1025:fzaaps>2.3.co;2

Camargo-Zanoguera, A., & Suarez-Reynoso, G. (1994). Evidencia sismica del crater impacto de Chicxulub. *BoltÍn de la Asociación Mexicana de Geofisicos de Exploracion*, *34*, 1–28.

Campos-Enriquez, J. O., Chavez-Garcia, F. J., Cruz, H., Acosta-Chang, J. G., Matsui, T., Arzate, J. A., et al. (2004). Shallow crustal structure of Chicxulub impact crater imaged with seismic, gravity and magnetotelluric data: Inferences about the central uplift. *Geophysical Journal International*, *157*(2), 515–525. https://doi.org/10.1111/j.1365-246x.2004.02243.x

Canales-Garcia, I., Urrutia-Fucugauchi, J., & Aguayo-Camargo, E. (2018). Seismic imaging and attribute analysis of Chicxulub crater central sector, Yucatan platform, Gulf of Mexico. *Geológica Acta*, *16*(2), 215–235.

Catchings, R. D., Powars, D. S., Gohn, G. S., Horton Jr, J. W., Goldman, M. R., & Hole, J. A. (2008). Anatomy of the Chesapeake Bay impact structure revealed by seismic imaging, Delmarva Peninsula, Virginia, USA. *Journal of Geophysical Research*, *113*(B8). https://doi.org/10.1029/2007jb005421

Christensen, N. I. (1996). Poisson's ratio and crustal seismology. *Journal of Geophysical Research*, *101*(B2), 3139–3156. https://doi.org/10.1029/95jb03446

Christeson, G. L., Collins, G. S., Morgan, J. V., Gulick, S. P., Barton, P. J., & Warner, M. R. (2009). Mantle deformation beneath the Chicxulub impact crater. *Earth and Planetary Science Letters*, *284*(1-2), 249-257.

Christeson, G. L., Gulick, S. P. S., Morgan, J. V., Gebhardt, C., Kring, D. A., Le Ber, E., et al. (2018). Extraordinary rocks from the peak ring of the Chicxulub impact crater: P-wave velocity, density, and porosity measurements from IODP/ICDP expedition 364. *Earth and Planetary Science Letters*, *495*, 1–11. https://doi.org/10.1016/j.epsl.2018.05.013

Christeson, G. L., Morgan, J. V., & Gulick, S. P. S. (2021). Mapping the Chicxulub impact stratigraphy and peak ring using drilling and seismic data. *Journal of Geophysical Research: Planets*, e2021JE006938. https://doi.org/10.1029/2021je006938

Christeson, G. L., Nakamura, Y., Buffler, R. T., Morgan, J., & Warner, M. (2001). Deep crustal structure of the Chicxulub impact crater. *Journal of Geophysical Research: Solid Earth*, *106*(B10), 21751–21769. https://doi.org/10.1029/2001jb000337

Cochran, E. S., Li, Y.-G., Shearer, P. M., Barbot, S., Fialko, Y., & Vidale, J. E. (2009). Seismic and geodetic evidence for extensive, long-lived fault damage zones. *Geology*, *37*(4), 315–318. https://doi.org/10.1130/g25306a.1

Collins, G. S. (2014). Numerical simulations of impact crater formation with dilatancy. *Journal of Geophysical Research: Planets*, *119*(12), 2600–2619. https://doi.org/10.1002/2014je004708

Collins, G. S., Melosh, H. J., & Ivanov, B. A. (2004). Modeling damage and deformation in impact simulations. *Meteoritics & Planetary Sciences*, *39*(2), 217–231. https://doi.org/10.1111/j.1945-5100.2004.tb00337.x

Collins, G. S., Melosh, H. J., Morgan, J. V., & Warner, M. R. (2002). Hydrocode simulations of Chicxulub crater collapse and peak-ring formation. *Icarus*, *157*(1), 24–33. https://doi.org/10.1006/icar.2002.6822

Collins, G. S., Morgan, J., Barton, P., Christeson, G. L., Gulick, S., Urrutia, J., et al. (2008). Dynamic modeling suggests terrace zone asymmetry in the Chicxulub crater is caused by target heterogeneity. *Earth and Planetary Science Letters*, *270*(3–4), 221–230. https://doi.org/10.1016/j.epsl.2008.03.032

Cooper, M. R., Kovach, R. L., & Watkins, J. S. (1974). Lunar near-surface structure. *Reviews of Geophysics*, *12*(3), 291–308. https://doi.org/10.1029/rg012i003p00291

Dainty, A. M., & Toksoz, M. N. (1977). Elastic wave-propagation in a highly scattering medium - Diffusion approach. *Journal of Geophysics-Zeitschrift Fur Geophysik*, *43*(1–2), 375–388.

de Graaff, S. J., Kaskes, P., Déhais, T., Goderis, S., Debaille, V., Ross, et al. (2021). *New insights into the formation and emplacement of impact melt rocks within the Chicxulub impact structure, following the 2016 IODP-ICDP Expedition 364"*. GSA Bulletin.

Dickmann, T. (2020). Using seismic exploration to predict geological risk along tunnels and underground spaces. *Proceedings of the Institution of Civil Engineers-Civil Engineering*, *173*(5), 11–16. https://doi.org/10.1680/jcien.19.00030

Dunn, M. L., & Ledbetter, H. (1995). Poissons ratio of porous and microcracked solids - Theory and application to oxide superconductors. *Journal of Materials Research*, *10*(11), 2715–2722. https://doi.org/10.1557/jmr.1995.2715

Eberli, G. P., Baechle, G. T., Anselmetti, F. S., & Incze, M. L. (2003). Factors controlling elastic properties in carbonate sediments and rocks. *The Leading Edge*, *22*(7), 654–660. https://doi.org/10.1190/1.1599691

Feignon, J. G., FerriÈre, L., Leroux, H., & Koeberl, C. (2020). Characterization of shocked quartz grains from Chicxulub peak ring granites and shock pressure estimates. *Meteoritics & Planetary Sciences*, *55*(10), 2206–2223. https://doi.org/10.1111/maps.13570

Filiberto, J., & Schwenzer, S. P. (2018). *Volatiles in the martian crust*. Elsevier.

French, R. H., & Hokett, S. L. (1998). *Evaluation of recharge potential at crater U5a (WISHBONE)*. Desert Research Institute, University and Community College System of Nevada.

Ganley, D. C. (1981). A method for calculating synthetic seismograms which include the effects of absorption and dispersion. *Geophysics*, *46*(8), 1100–1107. https://doi.org/10.1190/1.1441250

Gischler, E., & Lomando, A. J. (1999). Recent sedimentary facies of isolated carbonate platforms, Belize-Yucatan system, Central America. *Journal of Sedimentary Research*, *69*(3), 747–763. https://doi.org/10.2110/jsr.69.747

Glombick, P., Schmitt, D. R., Xie, W., Bown, T., Hathway, B., & Banks, C. (2014). The Bow City structure, southern Alberta, Canada: The deep roots of a complex impact structure? *Meteoritics & Planetary Sciences*, *49*(5), 872–895. https://doi.org/10.1111/maps.12296

Goderis, S. (2019). The final settling of meteoritic matter on the peak-ring of the Chicxulub impact structure at Site M0077 of IODP-ICDP Expedition 364. *Large Meteorite Impacts and Planetary Evolution IV*.

Goderis, S., Sato, H., Ferrière, L., Schmitz, B., Burney, D., Kaskes, P., et al. (2021). Globally distributed iridium layer preserved within the Chicxulub impact structure. *Science Advances*, *7*(9), eabe3647. https://doi.org/10.1126/sciadv.abe3647

Golos, E. M., Fang, H., & van der Hilst, R. D. (2020). Variations in seismic wave speed and VP/VS ratio in the North American lithosphere. *Journal of Geophysical Research: Solid Earth*, *125*(12), e2020JB020574. https://doi.org/10.1029/2020jb020574

Grady, D. E., & Kipp, M. E. (1987). *10 - Dynamic rock fragmentation. Fracture mechanics of rock* (pp. 429–475). Academic Press. https://doi.org/10.1016/b978-0-12-066266-1.50015-6

Gudlaugsson, S. T. (1993). Large impact crater in the Barents Sea. *Geology*, *21*(4), 291–294. https://doi.org/10.1130/0091-7613(1993)021<0291:licitb>2.3.co;2

Guerin, G., & Goldberg, D. (1996). Acoustic and elastic properties of calcareous sediments across a siliceous diagenetic front on the eastern US continental slope. *Geophysical Research Letters*, *23*(19), 2697–2700. https://doi.org/10.1029/96gl02188

Gulick, S., Christeson, G. L., Barton, P., Grieve, R., Morgan, J., & Urrutia-Fucugauchi, J. (2013). Geophysical characterization of the Chicxulub impact crater. *Reviews of Geophysics*, *51*(1), 31–52. https://doi.org/10.1002/rog.20007

Gulick, S., Morgan, J., & Mellett, C. (2016). *Expedition 364 preliminary report: Chicxulub: Drilling the K-pg impact crater*.

Gulick, S. M., Morgan, J., Mellett, C. L., Green, S. L., Bralower, T., Chenot, E., et al. (2017a). Chicxulub: Drilling the K-Pg impact crater. In *Proceedings of the International Ocean Discovery program*. ECORD. 364.

Gulick, S. M., Morgan, J., Mellett, C. L., Green, S. L., Bralower, T., Chenot, E., et al. (2017b). Expedition 364 methods. *Proceedings of the International Ocean Discovery Program*, 364. https://doi.org/10.14379/iodp.proc.364.102.2017

Gulick, S. M., Morgan, J., Mellett, C. L., Green, S. L., Bralower, T., Chenot, E., et al. (2017c). Site M0077: Lower peak ring. *Proceedings of the International Ocean Discovery Program*, *364*, 26. https://doi.org/10.14379/iodp.proc.364.107.2017

Gulick, S. M., Morgan, J., Mellett, C. L., Green, S. L., Bralower, T., Chenot, E., et al. (2017d). Site M0077: Open hole. *Proceedings of the International Ocean Discovery Program*, *364*, 26. https://doi.org/10.14379/iodp.proc.364.104.2017

Gulick, S. M., Morgan, J., Mellett, C. L., Green, S. L., Bralower, T., Chenot, E., et al. (2017e). Site M0077: Post-impact sedimentary rocks. *Proceedings of the International Ocean Discovery Program*, *364*. https://doi.org/10.14379/iodp.proc.364.105.2017

Gulick, S. P., Barton, P. J., Christeson, G. L., Morgan, J. V., McDonald, M., Mendoza-Cervantes, K., et al. (2008). Importance of pre-impact crustal structure for the asymmetry of the Chicxulub impact crater. *Nature Geoscience*, *1*(2), 131–135. https://doi.org/10.1038/ngeo103

Gulick, S. P., Bralower, T. J., Ormö, J., Hall, B., Grice, K., Schaefer, B., et al. (2019). The first day of the Cenozoic. *Proceedings of the National Academy of Sciences*, *116*(39), 19342–19351. https://doi.org/10.1073/pnas.1909479116

Gulick, S. P., Morgan, J. V., Mellett, C. L., Green, S. & Kring, D. A. (2017). *Site M0077: Open hole*, International Ocean Discovery Program.

Gulley, A. K., Eccles, J. D., Kaipio, J. P., & Malin, P. E. (2017). The effect of gradational velocities and anisotropy on fault-zone trapped waves. *Geophysical Journal International*, *210*(2), 964–978. https://doi.org/10.1093/gji/ggx200

Hamilton, E. L. (1979). Vp/Vs and Poisson ratios in marine-sediments and rocks. *Journal of the Acoustical Society of America*, *66*(4), 1093–1101. https://doi.org/10.1121/1.383344

Hardage, B. A. (1985). *Vertical seismic profiling*. Geophysical Press London.

Hauri, E. H., Saal, A. E., Rutherford, M. J., & Van Orman, J. A. (2015). Water in the Moon's interior: Truth and consequences. *Earth and Planetary Science Letters*, *409*, 252–264. https://doi.org/10.1016/j.epsl.2014.10.053

Heap, M. J., Gilg, H. A., Byrne, P. K., Wadsworth, F. B., & Reuschle, T. (2020). Petrophysical properties, mechanical behaviour, and failure modes of impact melt-bearing breccia (suevite) from the Ries impact crater (Germany). *Icarus*, *349*, 16. https://doi.org/10.1016/j.icarus.2020.113873

Hildebrand, A., Pilkington, M., Ortiz-Aleman, C., Chavez, R., Urrutia-Fucugauchi, J., Connors, M., et al. (1998). Mapping Chicxulub crater structure with gravity and seismic reflection data. *Geological Society, London, Special Publications*, *140*(1), 155–176. https://doi.org/10.1144/gsl.sp.1998.140.01.12

Hill, R. (1952). The elastic behaviour of a crystalline aggregate. *Proceedings of the Physical Society Section A*, *65*, 349–354. https://doi.org/10.1088/0370-1298/65/5/307

Hinds, R. C., Anderson, N. L., & Kuzmiski, R. D. (1996). *VSP interpretive processing: Theory and practice*. Society of Exploration Geophysicists.

Honniball, C., Lucey, P., Li, S., Shenoy, S., Orlando, T., Hibbitts, C., et al. (2021). Molecular water detected on the sunlit Moon by SOFIA. *Nature Astronomy*, *5*(2), 121–127. https://doi.org/10.1038/s41550-020-01222-x

Hunze, S., & Wonik, T. (2007). Lithological and structural characteristics of the Lake Bosumtwi impact crater, Ghana: Interpretation of acoustic televiewer images. *Meteoritics & Planetary Sciences*, *42*, 779–792. https://doi.org/10.1111/j.1945-5100.2007.tb01074.x

Ireland, M. T., Goulty, N. R., & Davies, R. J. (2010). Influence of pore water chemistry on silica diagenesis: Evidence from the interaction of diagenetic reaction zones with polygonal fault systems. *Journal of the Geological Society*, *167*(2), 273–279. https://doi.org/10.1144/0016-76492009-049

Ishii, E., Sanada, H., Iwatsuki, T., Sugita, Y., & Kurikami, H. (2011). Mechanical strength of the transition zone at the boundary between opal-A and opal-CT zones in siliceous rocks. *Engineering Geology*, *122*(3–4), 215–221. https://doi.org/10.1016/j.enggeo.2011.05.007

Ivanov, B., & Kostuchenko, V. (1997). Block oscillation model for impact crater collapse. *Lunar and Planetary Science Conference*.

Ivanov, B. A., Deniem, D., & Neukum, G. (1997). Implementation of dynamic strength models into 2D hydrocodes: Applications for atmospheric breakup and impact cratering. *International Journal of Impact Engineering*, *20*(1–5), 411–430. https://doi.org/10.1016/s0734-743x(97)87511-2

Japsen, P. (1998). Regional velocity-depth anomalies, North Sea Chalk: A record of overpressure and neogene uplift and erosion. *AAPG Bulletin*, *82*(11), 2031–2074. https://doi.org/10.1306/00aa7bda-1730-11d7-8645000102c1865d

Juhlin, C., & Pedersen, L. (1987). Reflection seismic investigations of the Siljan impact structure, Sweden. *Journal of Geophysical Research*, *92*(B13), 14113–14122. https://doi.org/10.1029/jb092ib13p14113

Kanasewich, E. R. (1974). *Time series analysis in Geophysics*. University of Alberta Press.

Kanbur, Z., Louie, J. N., Chávez-Pérez, S., Plank, G., & Morey, D. (2000). Seismic reflection study of upheaval Dome, Canyonlands National Park, Utah. *Journal of Geophysical Research*, *105*(E4), 9489–9505. https://doi.org/10.1029/1999je001131

Karakostas, F., Schmerr, N., Maquire, R., Kim, D., Huang, Q., Kawamura, T., et al. (2020). *DI024-0010 - S-coda wave analysis of InSight seismic data to determine the scattering and intrinsic attenuation in the crust of Mars. AGU Fall Meeting. Online*. American Geophysical Union.

Kaskes, P., De Graaff, S. J., Déhais, T., Goderis, S., Feignon, J. G., Ferrière, L., et al. (2019). Geochemical and petrographic characterization of the suevite sequence within the IODP-ICDP Exp. 364 core of the Chicxulub peak ring. Large Meteorite Impacts and Planetary Evolution VI: Lunar and Planetary Institute Contribution 2136, abstract 5085.

Keiswetter, D., Black, R., & Steeples, D. (1996). Seismic reflection analysis of the Manson impact structure, Iowa. *Journal of Geophysical Research*, *101*(B3), 5823–5834. https://doi.org/10.1029/95jb03117

Kenkmann, T., Poelchau, M. H., & Wulf, G. (2014). Structural geology of impact craters. *Journal of Structural Geology*, *62*, 156–182. https://doi.org/10.1016/j.jsg.2014.01.015

Kennett, B. L. N. (1974). Reflections, rays, and reverberations. *Bulletin of the Seismological Society of America*, *64*(6), 1685–1696. https://doi.org/10.1785/bssa0640061685

Kneib, G. (1995). The statistical nature of the upper continental crystalline crust derived from in situ seismic measurements. *Geophysical Journal International*, *122*(2), 594–616. https://doi.org/10.1111/j.1365-246x.1995.tb07015.x

Kovach, R. L., & Watkins, J. S. (1973). Apollo 17 seismic profiling - Probing lunar crust. *Science*, *180*(4090), 1063–1064. https://doi.org/10.1126/science.180.4090.1063

Kring, D. A., Tikoo, S. M., Schmieder, M., Riller, U., Rebolledo-Vieyra, M., Simpson, S. L., et al. (2020). Probing the hydrothermal system of the Chicxulub impact crater. *Science Advances*, *6*(22), 9. https://doi.org/10.1126/sciadv.aaz3053

Lasue, J., Clifford, S. M., Conway, S. J., Mangold, N., Butcher, F. E. G., Filiberto, J., & Schwenzer, S. P. (2019). Chapter 7 - The hydrology of Mars including a potential Cryosphere. In *Volatiles in the martian crust* (pp. 185–246). Elsevier. https://doi.org/10.1016/b978-0-12-804191-8.00007-6

Latham, G. V., Ewing, M., Press, F., Sutton, G., Dorman, J., Nakamura, Y., et al. (1970). Passive seismic experiment. *Science*, *167*(3918), 455–457. https://doi.org/10.1126/science.167.3918.455

Li, M., Zhao, Y., Li, M., & Zhao, Y. (2014). In *Chapter 7 - Prestack seismic inversion and seismic attribute AnalysisGeophysical Exploration technology* (pp. 199–219). Elsevier. https://doi.org/10.1016/b978-0-12-410436-5.00007-1

Liu, C. L., & Ahrens, T. J. (1997). Stress wave attenuation in shock-damaged rock. *Journal of Geophysical Research*, *102*(B3), 5243–5250. https://doi.org/10.1029/96jb03891

Lofi, J., Smith, D., Delahunty, C., Le Ber, E., Brun, L., Henry, G., et al. (2018). Drilling-induced and logging-related features illustrated from IODP-ICDP Expedition 364 downhole logs and borehole imaging tools. *Scientific Drilling*, *24*, 1–13. https://doi.org/10.5194/sd-24-1-2018

Lognonne, P., Banerdt, W. B., Pike, W. T., Giardini, D., Christensen, U., Garcia, R. F., et al. (2020). Constraints on the shallow elastic and an elastic structure of Mars from InSight seismic data. *Nature Geoscience*, *13*(3), 213–220.

Lopez Ramos, E. (1975). *Geological summary of the yucatan Peninsula. The Gulf of Mexico and the caribbean* (pp. 257–282). Springer US. https://doi.org/10.1007/978-1-4684-8535-6_7

Lowery, C. M., Bralower, T. J., Owens, J. D., Rodríguez-Tovar, F. J., Jones, H., Smit, J., et al. (2018). Rapid recovery of life at ground zero of the end-Cretaceous mass extinction. *Nature*, *558*(7709), 288–291. https://doi.org/10.1038/s41586-018-0163-6

Mackenzie, G. D., Maguire, P. K. H., Denton, P., Morgan, J., & Warner, M. (2001). Shallow seismic velocity structure of the Chicxulub impact crater from modelling of Rg dispersion using a genetic algorithm. *Tectonophysics*, *338*(2), 97–112. https://doi.org/10.1016/s0040-1951(01)00123-8

Meadows, D., & Davies, R. J. (2009). Predicting porosity reduction due to silica diagenesis using seismic reflection data. *Marine and Petroleum Geology*, *26*(8), 1543–1553. https://doi.org/10.1016/j.marpetgeo.2008.09.006

Meillieux, D. (2009). *Wellbore seismic and core sample measurement analysis: Integrated geophysical study of the lake Bosumtwi impact structure, Ghana*. MSc, University of Alberta.

Meister, R., Robertson, E. C., Werre, R. W., & Raspet, R. (1980). Elastic-moduli of rock glasses under pressure to 8-kilobars and geophysical implications. *Journal of Geophysical Research*, *85*(NB11), 6461–6470. https://doi.org/10.1029/jb085ib11p06461

Melosh, H. J. (1989). *Impact cratering: A geologic process*. Oxford University Press.

Melosh, H. J., Ryan, E. V., & Asphaug, E. (1992). Dynamic fragmentation in impacts - Hydrocode simulation of laboratory impacts. *Journal of Geophysical Research*, *97*(E9), 14735–14759. https://doi.org/10.1029/92je01632

Molyneux, J. B., & Schmitt, D. R. (2000). Compressional-wave velocities in attenuating media: A laboratory physical model study. *Geophysics*, *65*(4), 1162–1167. https://doi.org/10.1190/1.1444809

Montalbetti, J. F., & Kanasewich, E. R. (1970). Enhancement of teleseismic body phases with a polarization filter. *Geophysical Journal International*, *21*(2), 119–129. https://doi.org/10.1111/j.1365-246x.1970.tb01771.x

Moos, D., & Zoback, M. D. (1983). Insitu studies of velocity in fractured crystalline rocks. *Journal of Geophysical Research*, *88*(NB3), 2345–2358. https://doi.org/10.1029/jb088ib03p02345

Morgan, J., Gulick, S., Mellett, C., Lofi, J., Chenot, E., Christeson, G., et al. (2017). Chicxulub: Drilling the K-Pg impact crater. *Proceedings of the International Ocean Discovery Program*, *364*, 12. https://doi.org/10.14379/iodp.proc.364.2017

Morgan, J., Warner, M., Brittan, J., Buffler, R., Camargo, A., Christeson, G., et al. (1997). Size and morphology of the Chicxulub impact crater. *Nature*, *390*(6659), 472–476. https://doi.org/10.1038/37291

Morgan, J., Warner, M., Collins, G., Grieve, R., Christeson, G. L., Gulick, S., & Barton, P. (2011). Full waveform tomographic images of the peak ring at the Chicxulub impact crater. *Journal of Geophysical Research*, *116*(B6). https://doi.org/10.1029/2010jb008015

Morgan, J., Warner, M., Collins, G., Melosh, H., & Christeson, G. L. (2000). Peak-ring formation in large impact craters: Geophysical constraints from Chicxulub. *Earth and Planetary Science Letters*, *183*(3–4), 347–354. https://doi.org/10.1016/s0012-821x(00)00307-1

Morgan, J. V., Gulick, S. P., Bralower, T., Chenot, E., Christeson, G., Claeys, P., et al. (2016). The formation of peak rings in large impact craters. *Science*, *354*(6314), 878–882. https://doi.org/10.1126/science.aah6561

Moser, D., Poelchau, M. H., Stark, F., & Grosse, C. (2013). Application of nondestructive testing methods to study the damage zone underneath impact craters of MEMIN laboratory experiments. *Meteoritics & Planetary Sciences*, *48*(1), 87–98. https://doi.org/10.1111/maps.12000

Niessen, F., Gebhardt, A., Kopsch, C., & Wagner, B. (2007). Seismic investigation of the El'gygytgyn impact crater lake (central Chukotka, NE Siberia): Preliminary results. *Journal of Paleolimnology*, *37*(1), 49–63.

Nixon, C. (2021). *Replication data for "borehole seismic observations from the Chicxulub impact drilling: Implications for seismic reflectivity and impact damage*. UAL Dataverse. [V1]. https://doi.org/10.7939/DVN/D1YY4A

Nixon, C., Kofman, R., Schmitt, D. R., Gulick, S., Christesen, G., Saustraup, S., et al. (2020). *Assessment of rock damage using seismic methods: Wave speeds and attenuation from borehole measurements in the Chicxulub impact structure. 54th U.S. Rock mechanics/geomechanics symposium*(p. 8). American Rock Mechanics Association.

Njiekak, G., & Schmitt, D. R. (2019). Effective stress coefficient for seismic velocities in carbonate rocks: Effects of pore characteristics and fluid Types. *Pure and Applied Geophysics*, *176*(4), 1467–1485. https://doi.org/10.1007/s00024-018-2045-0

Nobes, D. C., Murray, R. W., Kuramoto, S. i., Pisciotto, K. A., & Holler, P. (1992). Impact of silica diagenesis on physical property variations. In *Proceedings of the ocean drilling program, scientific results*. Ocean Drilling Program. https://doi.org/10.2973/odp.proc.sr.127128.111.1992

O'Connell, R. J., & Budiansky, B. (1974). Seismic velocities in dry and saturated cracked solids. *Journal of Geophysical Research*, *79*(35), 5412–5426. https://doi.org/10.1029/jb079i035p05412

Okeefe, J. D., & Ahrens, T. J. (1993). Planetary cratering mechanics. *Journal of Geophysical Research*, *98*(E9), 17011–17028.

Ormö, J., Gulick, S. P., Whalen, M., King Jr, D., Sturkell, E., & Morgan, J. V. (2021). Assessing event magnitude and target water depth for marine-target impacts: Ocean resurge deposits in the Chicxulub M0077A drill core compared. *Earth and Planetary Science Letters*, *564*, 116915.

Osinski, G. R., Grieve, R. A., Hill, P. J., Simpson, S. L., Cockell, C., Christeson, G. L., et al. (2020). Explosive interaction of impact melt and seawater following the Chicxulub impact event. *Geology*, *48*(2), 108–112. https://doi.org/10.1130/g46783.1

Paillet, F. L., & Cheng, C. H. (1991). *Acoustic waves in boreholes*. CRC Press.

Pandit, B. I., & Tozer, D. C. (1970). Anomalous propagation of elastic energy within moon. *Nature*, *226*(5243), 335. https://doi.org/10.1038/226335a0

Phillips, R. J., Arvidson, R. E., Boyce, J. M., Campbell, D. B., Guest, J. E., Schaber, G. G., & Soderblom, L. A. (1991). Impact craters on venus: Initial analysis from magellan. *Science*, *252*(5003), 288–297. https://doi.org/10.1126/science.252.5003.288

Pike, R. J., & Spudis, P. D. (1987). Basin-ring spacing on the moon, mercury, and Mars. *Earth, Moon, and Planets*, *39*(2), 129–194. https://doi.org/10.1007/bf00054060

Pilkington, M., & Grieve, R. A. F. (1992). The geophysical signature of terrestrial impact craters. *Reviews of Geophysics*, *30*(2), 161–181. https://doi.org/10.1029/92rg00192

Pollack, J. B., Kasting, J. F., Richardson, S. M., & Poliakoff, K. (1987). The case for a wet, warm climate on early Mars. *Icarus*, *71*(2), 203–224. https://doi.org/10.1016/0019-1035(87)90147-3

Rae, A. S. P., Collins, G. S., Morgan, J. V., Salge, T., Christeson, G. L., Leung, J., et al. (2019). Impact-induced porosity and microfracturing at the Chicxulub impact structure. *Journal of Geophysical Research: Planets*, *124*(7), 1960–1978. https://doi.org/10.1029/2019je005929

Raith, M., Ebert, M., Pinkert, K., & Grosse, C. U. (2018). Nondestructive imaging of hypervelocity impact-induced damage zones beneath laboratory-created craters by means of ultrasound travel-time tomography. *Meteoritics & Planetary Sciences*, *53*(8), 1756–1772. https://doi.org/10.1111/maps.13113

Rempe, M., Mitchell, T., Renner, J., Nippress, S., Ben-Zion, Y., & Rockwell, T. (2013). Damage and seismic velocity structure of pulverized rocks near the San Andreas Fault. *Journal of Geophysical Research: Solid Earth*, *118*(6), 2813–2831. https://doi.org/10.1002/jgrb.50184

Rempe, M., Mitchell, T. M., Renner, J., Smith, S. A. F., Bistacchi, A., & Di Toro, G. (2018). The relationship between microfracture damage and the physical properties of fault-related rocks: The gole larghe fault zone, Italian southern Alps. *Journal of Geophysical Research: Solid Earth*, *123*(9), 7661–7687. https://doi.org/10.1029/2018jb015900

Riller, U., Poelchau, M. H., Rae, A. S. P., Schulte, F. M., Collins, G. S., Melosh, H. J., et al. (2018). Rock fluidization during peak-ring formation of large impact structures. *Nature*, *562*(7728), 511–518. https://doi.org/10.1038/s41586-018-0607-z

Salguero-Hernández, E., Pérez-Cruz, L., & Urrutia-Fucugauchi, J. (2020). Seismic attribute analysis of Chicxulub impact crater. *Acta Geophysica*.

Schmitt, D. R., Milkereit, B., Karp, T., Scholz, C., Danuor, S., Meillieux, D., & Welz, M. (2007). In situ seismic measurements in borehole LB-08A in the Bosumtwi impact structure, Ghana: Preliminary interpretation. *Meteoritics & Planetary Sciences*, *42*(4–5), 755–768. https://doi.org/10.1111/j.1945-5100.2007.tb01072.x

Scholz, C. A., Karp, T., Brooks, K. M., Milkereit, B., Amoako, P. Y., & Arko, J. A. (2002). Pronounced central uplift identified in the Bosumtwi impact structure, Ghana, using multichannel seismic reflection data. *Geology*, *30*(10), 939–942. https://doi.org/10.1130/0091-7613(2002)030<0939:pcuiit>2.0.co;2

Schubnel, A., Benson, P. M., Thompson, B. D., Hazzard, J. F., & Young, R. P. (2006). Quantifying damage, saturation and anisotropy in cracked rocks by inverting elastic wave velocities. In *Rock damage and fluid transport, part I* (pp. 947–973). Birkhäuser Basel. https://doi.org/10.1007/3-7643-7712-7_3

Schulte, F. M., Wittmann, A., Jung, S., Morgan, J. V., Gulick, S. P., Kring, D. A., et al. (2021). Ocean resurge-induced impact melt dynamics on the peak-ring of the Chicxulub impact structure, Mexico. *International Journal of Earth Sciences*, 1–18. https://doi.org/10.1007/s00531-021-02008-w

Scott, D., & Hajnal, Z. (1988). Seismic signature of the Haughton structure. *Meteoritics*, *23*(3), 239–247. https://doi.org/10.1111/j.1945-5100.1988.tb01287.x

Simpson, S. L., Osinski, G. R., Longstaffe, F. J., Schmieder, M., & Kring, D. A. (2020). Hydrothermal alteration associated with the Chicxulub impact crater upper peak-ring breccias. *Earth and Planetary Science Letters*, *547*, 116425. https://doi.org/10.1016/j.epsl.2020.116425

Sjogren, B., Ofsthus, A., & Sandberg, J. (1979). Seismic classification of rock mass qualities. *Geophysical Prospecting*, *27*(2), 409–442. https://doi.org/10.1111/j.1365-2478.1979.tb00977.x

Smith, V., Warny, S., Grice, K., Schaefer, B., Whalen, M. T., Vellekoop, J., et al. (2020). Life and death in the Chicxulub impact crater: A record of the Paleocene–eocene thermal Maximum. *Climate of the Past*, *16*(5), 1889–1899. https://doi.org/10.5194/cp-16-1889-2020

Stephen, R. A., & Harding, A. J. (1983). Travel time analysis of borehole seismic data. *Journal of Geophysical Research*, *88*(NB10), 8289–8298. https://doi.org/10.1029/jb088ib10p08289

Stewart, R. R. (1984). VSP interval velocities from traveltime inversion. *Geophysical Prospecting*, *32*(4), 608–628. https://doi.org/10.1111/j.1365-2478.1984.tb01709.x

Stierman, D. J., & Kovach, R. L. (1979). An in situ velocity study: The Stone Canyon Well. *Journal of Geophysical Research*, *84*(B2), 672–678. https://doi.org/10.1029/jb084ib02p00672

Swanson, E., Wilson, J., Broome, S., & Sussman, A. (2020). The complicated link between material properties and microfracture density for an underground explosion in granite. *Journal of Geophysical Research: Solid Earth*, *125*(11), 15. https://doi.org/10.1029/2020jb019894

Thurber, C. (2006). Three-dimensional compressional wavespeed model, earthquake relocations, and focal mechanisms for the Parkfield, California, region. *Bulletin of the Seismological Society of America*, *96*(4B), S38–S49. https://doi.org/10.1785/0120050825

Vermeesch, P. M., & Morgan, J. V. (2008). Structural uplift beneath the Chicxulub impact structure. *Journal of Geophysical Research*, *113*(B7), 10. https://doi.org/10.1029/2007jb005393

Wang, X. Q., Schubnel, A., Fortin, J., David, E. C., Guéguen, Y., & Ge, H. K. (2012). High Vp/Vs ratio: Saturated cracks or anisotropy effects? *Geophysical Research Letters*, *39*(11). https://doi.org/10.1029/2012gl051742

Weide, D. L., & Faber, M. L. (1985). *Soils and Quaternary geology of the southwestern United States*. Geological Society of America.

Whalen, M. T., Gulick, S. P., Lowery, C. M., Bralower, T. J., Morgan, J. V., Grice, K., et al. (2020). Winding down the Chicxulub impact: The transition between impact and normal marine sedimentation near ground zero. *Marine Geology*, *430*, 106368. https://doi.org/10.1016/j.margeo.2020.106368

Wiggins, S. E., Johnson, B. C., Bowling, T. J., Melosh, H. J., & Silber, E. A. (2019). Impact fragmentation and the development of the deep lunar megaregolith. *Journal of Geophysical Research: Planets*, *124*(4), 941–957. https://doi.org/10.1029/2018je005757

Wong, J., Hurley, P., & West, G. F. (1983). Crosshole seismology and seismic imaging in crystalline rocks. *Geophysical Research Letters*, *10*(8), 686–689. https://doi.org/10.1029/gl010i008p00686

Wood, C., & Head, J. (1976). Comparison of impact basins on mercury, Mars and the moon. *Lunar and Planetary Science Conference Proceedings*.

Wordsworth, R. D. (2016). The climate of early Mars. *Annual Review of Earth and Planetary Sciences*, *44*, 381–408. https://doi.org/10.1146/annurev-earth-060115-012355

Wu, J., Milkereit, B., & Boerner, D. E. (1995). Seismic imaging of the enigmatic Sudbury structure. *Journal of Geophysical Research*, *100*(B3), 4117–4130. https://doi.org/10.1029/94jb02647

Xia, K. W., & Ahrens, T. J. (2001). Impact induced damage beneath craters. *Geophysical Research Letters*, *28*(18), 3525–3527. https://doi.org/10.1029/2001gl013001

Zhao, J., Xiao, L., Gulick, S. P., Morgan, J. V., Kring, D., Fucugauchi, J. U., et al. (2020). Geochemistry, geochronology and petrogenesis of maya block granitoids and dykes from the Chicxulub impact crater, Gulf of México: Implications for the assembly of Pangea. *Gondwana Research*, *82*, 128–150. https://doi.org/10.1016/j.gr.2019.12.003